Stochastic near-surface wind field estimation from sparse aerial swarm measurements to support wildfire behaviour predictions

Mohammad Tavakol Sadrabadi[a], Mauro Sebastián Innocente[b,*]

[a]Centre for Future Transport and Cities, Coventry University, Coventry, UK
[b]SwarmMind Ltd, London, UK

ARTICLE INFO

Keywords:
Wind downscaling
Fire-induced wind
Fire dynamics simulator (FDS)
Physics-constrained Neural Networks
Fluid flow reconstruction

ABSTRACT

Wildfire behaviour is influenced by weather, fuel, and topography. Detailed physics-based simulations are computationally expensive, particularly if accounting for fire–wind interactions. To address this, simplified models are developed that disregard certain physical laws and are often decoupled from the atmosphere. Additionally, efforts to improve model reliability by feeding near-surface wind fields into the model using statistical and dynamical downscaling methods have two drawbacks: disregarding fire–wind interaction, and high computational demand of dynamical methods. This study proposes combining UAV-swarm-based wind and temperature measurements with convolutional neural networks to estimate the near-surface fire-induced wind field, aiming to capture the fire–wind interaction and its effect on fire propagation dynamics in grassland fires without solving Navier-Stokes equations. The two-step process includes (*i*) super-resolution reconstruction of high-altitude wind field from sparse UAV-based measurements, and (*ii*) high-resolution mapping of high-altitude to near-surface wind fields. The latter may be fed into decoupled wildfire models to replicate the effect of fire–wind interactions. Synthetic data is generated via LES simulations of grassland fires with different wind speeds, terrain slopes, vegetation types, and heights. The model performance is evaluated across different UAV swarm sizes, spatial UAV distributions, and wind measurement errors. Results suggest that the developed framework accurately estimates the near-surface wind field, even with a limited number of UAVs, achieving average MAE and RMSE values of 0.849 and 1.323 for U, 0.672 and 1.022 for V, and 0.551 and 1.01 for W velocity components. Model uncertainty increases with smaller swarm sizes and higher measurement noise.

1. Introduction

In recent years, the frequency, scale, and severity of wildfires have increased globally as a result of the impacts of climate change [1, 2], urging the need for a comprehensive understanding of wildfire dynamics and their interaction with the atmosphere. Fire-atmosphere interaction refers to the complex interactions between a fire and the surrounding atmospheric environment, encompassing the interaction between the burning fuels and atmosphere, the energy and mass fluxes between dead and living vegetation, as well as the interaction between the atmosphere and the combustion process as long as the resultant perturbations are larger than the normal ambient variability [3, 4]. A critical aspect of fire-atmosphere interaction considers the effect of wind on the fire dynamics, as understanding this effect is central to comprehensively capturing the feedback mechanisms between fire and atmosphere.

1.1. Fire-wind interaction

During the past century, numerous studies have highlighted the influence of the ambient and ground-level wind on fire growth dynamics. Gisborne [5] noted that the wind contributes to fire propagation through four mechanisms: (*i*) enhancing moisture exchange between vegetation and atmosphere, (*ii*) increasing the rate of spread of fire, (*iii*) carrying ignited embers to unburnt areas, and (*iv*) supplying oxygen flux into the flaming front. By tilting the flame, the ambient wind also reduces the distance between the flame and the fuel bed and enhances radiative and convective heat transfer to the unburnt vegetation [3, 6].

*Corresponding author
tavakolsam@uni.coventry.ac.uk (M. Tavakol Sadrabadi); mauro.s.innocente@swarmmind.uk (M.S. Innocente)
pureportal.coventry.ac.uk/en/persons/mohammad-tavakol-sadrabadi (M. Tavakol Sadrabadi); https://swarmmind.uk/ (M.S. Innocente)
ORCID(s): 0000-0002-5938-6310 (M. Tavakol Sadrabadi); 0000-0001-8836-2839 (M.S. Innocente)

Wildfires, in turn, alter their surrounding environment by releasing a considerable amount of heat, which induces buoyant updrafts, as well as lateral indrafts [7] and horizontal vortices surrounding the plume[4]. Hence, a precise identification of the turbulent structure and momentum fluxes surrounding the fire is important, as they cause spatial and temporal changes in fire spread [8]. Even low-intensity fires may produce atmospheric turbulence that affects the fire front dynamics (i.e. see [9]). Consequently, a considerable number of studies have focused on characterising turbulence in the vicinity of fires through large-scale experiments such as the International Crown Fire Modelling Experiment ($ICFME$) [10], field-scale experiments (i.e. see [11]), and small-scale experiments such as [12]. Additionally, some studies, such as [13, 14, 15] have further attempted to provide a detailed description of the coupled fire atmosphere interaction utilising numerical simulations.

Given the multi-scale nature of wildfires, the physics and dynamics of the models highly depend on the desired temporal and spatial scales, implying distinct sets of equations for various scales [16]. A group of models, often called *fully-coupled* models, such as FIRETEC [17] and *WFDS* [18], solve the complete set of fluid dynamics and thermochemical equations to capture the dynamics of a wildfire by accounting for changes in moisture, temperature, wind speed, and direction. Though such a detailed solution provides detailed insights into extreme events in wildfires, its applicability in operational fire management tasks is limited due to high computational costs [16].

To address the need for decision support tools capable of providing fast and large-scale estimations, a series of faster-than-real-time (FTRT) models such as FARSITE [19], BEHAVE [20], and FireProM-F [21, 22] are developed. These models are partially or fully decoupled from the wind to limit the computation demands. Yet as a result, these models' uncertainty level increases significantly for longer estimation intervals [16]. To mitigate the uncertainty, a series of studies have focused on utilising data assimilation techniques [23], or incorporating numerical weather prediction (*NWP*) models into fire propagation models [24]. Nonetheless, their suitability is questionable as large-scale models may not capture the impact of smaller-scale fires. The large-scale outputs from NWP models, however, should be downscaled to better reflect the fine-scale dynamics in complex terrains before being input into fire models.

1.2. Wind downscaling

Downscaling refers to the process of obtaining fine-scale quantities from lower-resolution data using appropriate refinement methods [25]. Traditionally, wildland fire decision support systems utilise large-scale meteorological forecasts to generate a domain-average wind field for fire propagation forecasting [26]. Still, small-scale wind dynamics play a major role in fire behaviour. Consequently, several studies have focused on generating more refined wind maps to enhance the accuracy of wildfire modelling. Forthofer et al. [26, 27] compared the effect of three techniques for generating fine-scale surface winds from *NWP* models on fire propagation estimations. These methods include(i) a uniform wind field over the train, (ii) utilising 2D mass-conserving models [28, 29], and (iii) utilising Mass and momentum-conserving numerical models for wind field downscaling. Their results indicated that high-resolution wind input increases the accuracy of fire propagation estimations, with accuracy increasing alongside the complexity of the model.

Downscaling methods can be classified into (i) dynamical and (ii) empirical-statistical approaches [30]. Dynamical downscaling employs high-resolution mass-conserving or momentum-conserving models to interpret the outputs of *NWP* models on a finer scale. This method, however, is computationally expensive and time-consuming, so it is typically restricted to small domains [25]. In contrast, statistical approaches train statistical models on pair quantities at coarse and fine scales, to enable instant or real-time estimations due to the minimal inference times of statistical models.

Recent advancements in machine learning (ML) and deep learning (DL) methods facilitated the use of the state-of-the-art algorithms for wind downscaling studies [see 31, 32]. In particular, Convolutional Neural networks (CNN) and single image super-resolution (SR) methods [see 33, 34] have proven to be effective due to their capabilities in learning multidimensional mappings. They are particularly useful when spatially distributed data and the generation of high-resolution data from low-resolution inputs are of interest [25].

This super-resolution procedure is generally referred to as flow field reconstruction within the context of flow mechanics literature. An example would be to interpret a low-resolution fluid flow image (data matrix) as a collection of sparse sensor measurements. Utilising such an approach, super-resolution analysis could be extended to address the inverse problem of reconstructing global fields from local observations [35]. Different studies have utilised various deep-learning models for flow field reconstruction purposes. Examples include convolutional neural networks mostly with UNet structures (i.e. see [36, 37]), artificial neural networks with autoencoder architectures [38], and physics-informed frameworks [31, 39].

While deep learning and machine learning models are frequently used for various types of inference and decision-making procedures, assessing the effectiveness and reliability of these AI systems before deploying and utilising them is crucial.

1.3. Uncertainty estimation for flow field reconstruction

Uncertainty quantification (UQ) forms the basis of many important decisions, and predictions without UQ are typically unreliable [40]. UQ methods could be categorised into (*i*) Bayesian methods and (*ii*) ensemble methods [40]. Bayesian methods encompass techniques such as the Markov chain Monte-Carlo (MCMC) algorithm, variational inference methods (VI), Monte-Carlo dropout (MCD), etc [40]. While principled, methods like Bayesian neural networks, MCMC, and the ensemble of models are computationally expensive and hence impractical for large datasets and applications [40, 41]. As a result, approximation techniques such as MCD [42] and Monte-Carlo batch normalisation (MCBN) [43], which could be used to estimate the epistemic uncertainty of a single trained model, have gained traction. MCD leverages dropout during inference to generate an ensemble of outputs from a single model, effectively sampling from a predictive distribution and estimating its mean and variance [42, 41]. MCBN is another technique that could be used to approximate the Bayesian inference in neural networks [43]. In this approach, many mini-batches are created by selecting random samples to go along with a particular query during inference. The predictive distribution is then estimated using the mean and variance of the ensemble of outputs [41].

While high-resolution wind data significantly enhances fire spread modelling accuracy, acquiring such data efficiently is challenging or virtually infeasible. However, recent advancements in unmanned aerial vehicles technology offer promising localised and real-time data collection capabilities, which would help overcome these scale and resolution limitations in the dynamic environment of wildfire.

1.4. Drones in wildfire management activities

Recent advancements in UAV technology offer valuable capabilities to the fire community, including real-time fire detection, monitoring, and fighting assistance [see 44]. They are typically equipped with sensors such as the Global Navigation Satellite System (GNSS), Inertial Navigation System (INS), and at least one imagery sensor [45] and offer mobility in three dimensions, which makes them flexible and cost-effective instruments for providing spatiotemporal measurements, such as the atmospheric wind [46]. As a result, an increased number of studies have focused on the use of UAVs for wind field measurement tasks over other conventional alternatives such as wind LiDARs, balloons, and wind measurement towers (e.g., [see 47, 48]). Both fixed-wing and rotary-wing UAVs could be used for atmospheric wind measurements, with fixed-wing UAVs more suited to measurement tasks that cover large areas and rotary-wing UAVs mostly suitable for measurements that need hovering on a spot for long periods, such as validating wind measurements and in the proximity of the structures [46]. Wind measurements could be performed using external wind sensors or onboard avionic systems [49]. The idea of coordinated wind measurement with multiple UAVs was first proposed by [50], and later implemented in the field by [49], which utilised a group of quadrotors hovering for a long period at certain locations, to provide spatiotemporal wind measurements.

1.5. Contribution

Reviewing the literature, it could be inferred that recent efforts to reduce uncertainty in operational wildfire models have focused on incorporating the high-resolution near-surface wind field in them, utilising various dynamical and statistical methods. Although effective to some extent, two limitations remain unaddressed.

- Dynamic downscaling, though faster than executing a fully coupled simulation, requires significant processing capacity, especially for large territories.
- Both downscaling methods rely on the outputs of NWP models or synoptic measurements and often fail to capture the enhancing effect of fire on the surrounding atmosphere, particularly for smaller-scale fires.

To address these issues, [51] proposed a methodology based on combining real-time *UAV*-swarm-based wind measurements above the fire with deep neural networks to reconstruct the high-resolution near-surface wind field. This method estimates near-surface wind fields from sparse UAV-based measurements at higher altitudes and offers the ability to improve the predictions of the wildfire model by inputting estimated wind fields to the wildfire model. Hence, it effectively mimics the fire–wind interaction without incurring the hefty cost of solving the Navier-Stokes equations [51]. This paper builds on that concept, focusing on the detailed development of the wind reconstruction

pipeline, including details on synthetic data generation, model architecture design, evaluation, as well as the uncertainty quantification procedure.

The remainder of this paper is organised as follows: Section 2 provides an overview of the introduced framework and its building blocks; Section 3 presents details on model development, simulation configurations, dataset preparation, and AI models architecture and training procedures; Section 4 provides the results of the model training, including model performance metrics, and uncertainty evaluations for high altitude wind field reconstruction (Section 4.1) and near-surface wind field estimation (Section 4.2), respectively; Sections 5 shortly discussses practical capabilities and limitations of the system; and finally Section 6 provides a summary of the research findings and derived conclusions.

2. System description

This paper presents a data-driven system for downscaling wind patterns in the vicinity of grassland fires to improve the accuracy and reduce the uncertainty of fire spread predictions, utilising real-time measurements from a swarm of UAVs. A schematic of the system is presented in Figure 1. Given that the fire plume typically tilts forward due to the ambient wind velocity, the turbulent fields near the surface and at the measurement height differ significantly. Therefore, downscaling atmospheric turbulence in the presence of fire cannot be directly addressed through a single-image super-resolution similar to typical downscaling studies. To address this, the proposed system consists of three key steps:

- Real-time UAV-swarm-based measurement of the turbulent wind above the fire;
- Reconstruction of high-resolution wind field at UAV flight altitude from sparse measurements;
- Estimation of high-resolution near-surface wind field from the reconstructed wind at UAV altitude

It is important to note that while the *downscaling* often refers solely to super-resolution or reconstruction step in the literature, this study considers downscaling to encompass both the super-resolution/reconstruction step and the estimation of the high-resolution near-surface wind field from the reconstructed high-altitude wind field. A schematic description of the proposed methodology is presented in Figure 2.

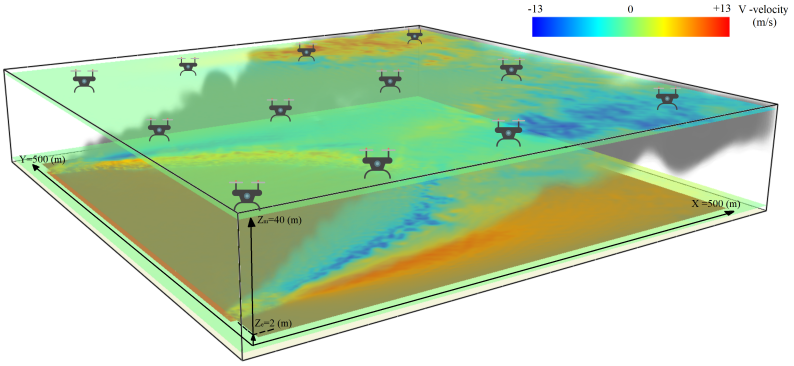

Figure 1: Schematic view of the fire propagation and distribution of the transverse component of velocity (V) at 2m *AGL* and 40m *AGL* along with the *UAV* swarm .

The first component of the system is the *UAV* swarm, responsible for the measurement of wind and temperature at the determined flight height (Z_m–assumed to be equal to 40 m above ground level (*AGL*). The swarm is also responsible for monitoring the location and temperature of the fire front. Depending on the type of UAV, a variety of sensors such as pitot tubes and multi-hole pressure probes, mechanical and sonic anemometers, or LiDAR systems could be used. While these sensors mounted on quadrotors are reported to introduce measurement errors of up to 50% [52], adequate sampling strategies such as the Nyquist sampling theorem should be fulfilled to mitigate aliasing problems and capture the signal effectively. This is, however, more problematic when using fixed-wind UAVs, which normally fly at higher speeds (e.g. see [53]).

The downscaling process is then addressed through a two-stage convolutional neural network pipeline. The first utilises the sparsely measured wind values at each time step as input to generate a high-resolution map of the wind field

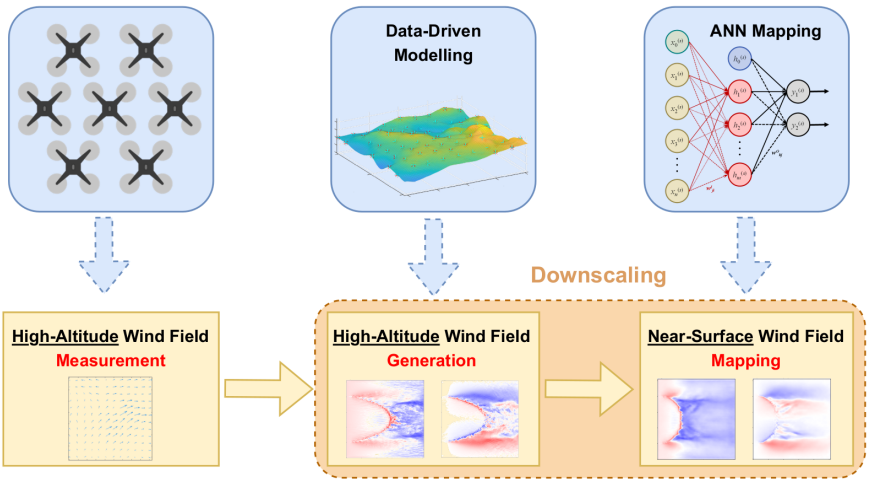

Figure 2: Schematic description of the proposed methodology adopted and modified from [51]

Table 1
Overview of the simulated Geometric and physical properties of the vegetation, terrain, and wind

Veg model	Veg height (m)	Terrain Slope (degrees)	U_{10} (m/s)	N. simulations
Veg_1	0.2, 0.5, 10	-40%(-21.8) , -20%(-11.31) , 0 (0), +20%(-11.31), +40%(-21.8)	4, 6, 8, 10, 12	75
Veg_2	0.2, 0.5, 10	-40%(-21.8) , -20%(-11.31) , 0 (0), +20%(-11.31), +40%(-21.8)	4, 6, 8, 10, 12	75

at the measurement altitude (Z_m=40 m). The second model then estimates the near-surface wind field (Z_e=2 m *AGL*) through an image-to-image translation model. This separation was found effective in allowing the model to capture the dynamics of fire-induced turbulent field while keeping the model size and architecture efficient.

3. Materials and Methods

Training deep learning models requires an extensive amount of data, while actual measurements of wind velocity in wildfire situations are challenging. Hence, this study generates synthetic training data through performing 150 three-dimensional computational fluid dynamics (CFD) simulations of wildland fire propagation in different scenarios. All simulations are performed utilising the Fire Dynamics Simulator (FDS), a solver of the Navier-Stokes equations appropriate for low-speed, thermally-driven flows developed by the National Institute of Standards and Technology (NIST)[54].

3.1. Simulation setup

An overview of the physical and geometrical parameters of the simulation conditions, including wind velocity, vegetation height and type, and terrain slope, is presented in Table 1. Each vegetation type is used in 75 simulations combining three vegetation heights (H_g), five terrain slopes (S), and five different ambient wind speeds (u_{10}).

The fuel is represented utilising the Lagrangian Particle Model (LPM) in FDS, which represents the fuel as a group of Lagrangian particles heated by convection-radiation heat transfer [54]. The specific physical and thermal parameters of fuels utilised in this study are presented in Table 2.

The ambient wind is introduced into the model utilising the Monin-Obukhov similarity theory, for which the wind speed (u_z) and potential temperature change with height as follows:

$$u(z) = \frac{u_*}{k}\left[ln\left(\frac{z}{z_o}\right) - \Psi_m\left(\frac{z}{L}\right)\right] \tag{1}$$

$$\theta(z) = \theta_0 + \frac{\theta_*}{k}\left[ln\left(\frac{z}{z_o}\right) - \Psi_h\left(\frac{z}{L}\right)\right] \tag{2}$$

Table 2
Summary of fuel physical properties and thermal decomposition coefficients

Property	Unit	Veg_1(Veg_2)	Reference
Area to Volume Ratio (σ)	m^{-1}	9,770	[55]
Bulk density (ρ_b)	$kg.m^{-3}$	1.313	[55]
Fuel	-	Cellulose	[15]
Fuel Density (ρ)	$kg.m^{-3}$	512	[15]
Moisture content (M)	%	6.3	[55]
Specific Heat	$kJ\ kg^{-1}\ K^{-1}$	2.1	[56]
Conductivity	$kJ\ kg^{-1}\ K^{-1}$	0.1	[15]
Heat of Evaporation (H_{H_2O})	$kJ\ kg^{-1}$	2259	[57]
Heat of Combustion (H_c)	$kJ\ kg^{-1}$	17,400	[54]
Heat of Pyrolysis (H_{pyr})	$kJ\ kg^{-1}$	418	[57]
A_{pyr}	s^{-1}	1040 (24550)	[58] ([59])
E_{pyr}	$J.mol^{-1}$	61041 (58200)	[58] ([59])
Char Yield (ν_{char})	$kg\ kg^{-1}$	0.25 (0.23)	[54]
A_{char}	$kg.m^{-2}.s^{-1}$	465	[60]
E_{char}	$J.mol^{-1}$	68000	[60]
Ash Yield (ν_{ash})	$kg\ kg^{-1}$	0.04	[54]
Obukhov Length (L)	m	−500	[15]
Roughness Length(z_0)	m	0.03	[15]
Drag Coefficient (c_d)	-	2.8	[54]
Soil Specific Heat	$kJ\ kg^{-1}\ K^{-1}$	2.0	[15]
Soil Conductivity	$W\ m^{-1}\ K^{-1}$	0.25	[15]
Soil Density	$kg\ m^{-3}$	1,300	[15]
Relative Humidity	%	40	[15]

Where u_* is the friction velocity, k is the von Karman constant equal to 0.41, z_0 is the aerodynamic roughness length, θ_* the scaling potential temperature, θ_0 ground level temperature, L is the Obukhov length, and Ψ_h and Ψ_m represent similarity functions. An unstable stratified condition is assumed to represent the conditions of a warm summer day aligned with the experimental conditions of the reference experiment.

The turbulent flow field is modelled utilising the very large eddy simulation (VLES) model with Deardorff's sub-grid scale (SGS) model for turbulent eddy viscosity closure terms. To replicate the natural turbulence of the atmospheric boundary layer, the synthetic eddy method (SEM)[61] with an arbitrary value of 10% turbulence intensity is used to introduce random eddies into the domain, following prior studies (i.e. see [62, 63]). Boundary Conditions include a no-slip boundary condition for the ground surface and 'Open' boundary conditions for the rest of the boundaries.

3.2. Grid sensitivity and model validation

Simulations are validated against field-scale experiments carried out by the Commonwealth Scientific and Industrial Research Organisation (CSIRO) during July and August 1986. The reference experiment here is the C064 experiment, carried out in a 100×100 m field covered with Kerosene grass. Experimental conditions include wind speed u_2=4.6 m/s, temperature T=32°C, and H_g=0.21 m, resulting in a rate of spread (RoS) of 1.2 m/s [55]. The fire was ignited by two field workers walking in opposite directions from the centre of the upwind boundary, modelled here as a strip of burnable grass with a specified RoS along the strip.

Grid sensitivity is studied by tracking the firefront location generated by different grid sizes over time under simulation conditions comparable to the actual experiment. As presented in Figure 3a, three different grid sizes of $1 \times 1 \times 1$ m^3 (coarse), $0.5 \times 0.5 \times 0.5$ m^3 (fine), and $0.25 \times 0.25 \times 0.25$ m^3 (very fine) were tested. Additionally, the effect of turbulence model on fire front location and heat release ratio (HRR) was studied, comparing the estimations from Simple Very Large Eddy Simulation (*SVLES*), Very Large Eddy Simulation (*VLES*), and Large Eddy Simulation (*LES*) models as depicted in Figure 3b and 3c for front location and HRR, respectively. Finally, Figure 3d compares the simulated wind speed with the measured data during the experiment. Though replicating the exact wind variations is inherently challenging, a general agreement could be observed between the simulation and the measured values.

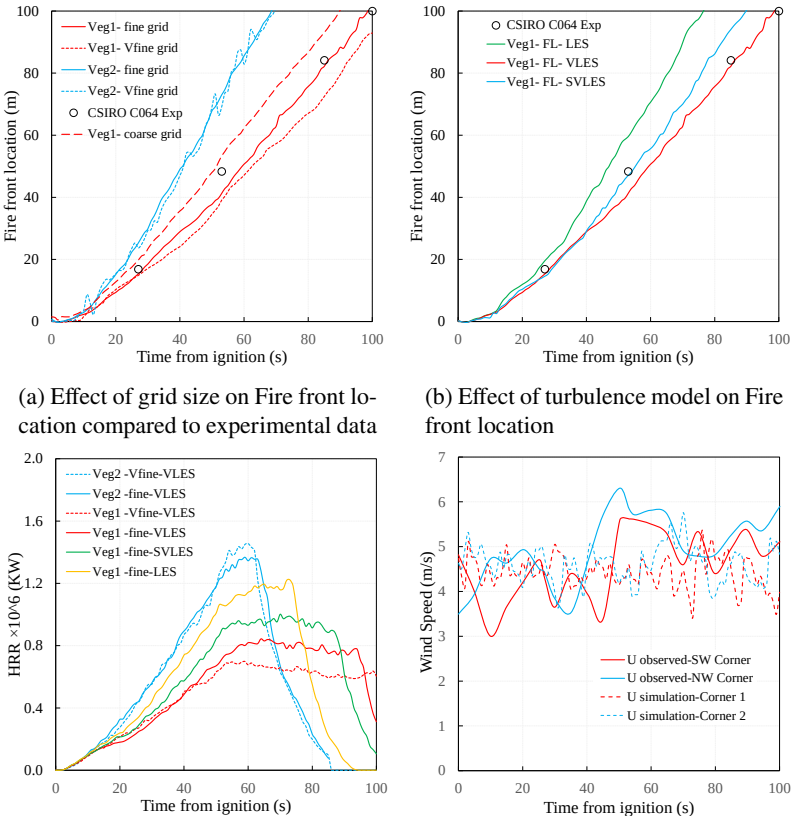

(a) Effect of grid size on Fire front location compared to experimental data

(b) Effect of turbulence model on Fire front location

(c) Effect of grid size and turbulence model on obtained HRR

(d) Comparison of measured and simulated wind velocity (U component) during the experiment

Figure 3: Model sensitivity and validation analysis

Even though the estimations of the fire-front location using a 0.5 m grid align with the experimental data, it may not be fine enough to adequately resolve a high fraction of the turbulent kinetic energy to ensure a valid Large Eddy Simulation. Consequently, a posteriori grid quality analysis is conducted, which includes studying the effect of grid size on turbulence characteristics by calculating the spectral density of turbulence and the measure of turbulence resolution $M(\mathrm{x})$ metric. The power spectral density (PSD) is useful in characterising kinetic energy distribution across different frequencies or scales of turbulent motion. Figure 4 presents the effect of grid size on the estimated spectral density (4a) and wind velocity (u_2) time series (4b) measured 9 meters downstream of a 10 MW/m pool fire with a width of 1 m. Data were sampled at 10 Hz for 260 seconds. The measurement point is located within the fire plume, so it reflects the fire-induced wind velocities. Results indicate that the simulated wind time series and the power spectral density distribution estimated using 0.5 and 0.25 m grid are comparable, suggesting that the 0.5 m grid can be sufficient. It should be highlighted that while the observed fire intensities in our experiments span a wide range, the 10 MW fire is chosen to represent an average intensity from across simulation scenarios. The measure of turbulence resolution could be calculated as follows [54]:

$$M(x) = \frac{k_{\mathrm{sgs}}}{k_{\mathrm{sgs}} + \mathrm{TKE}} \tag{3}$$

where TKE is the turbulent kinetic energy and could be calculated as follows:

$$\mathrm{TKE} = \frac{1}{2}\left((\overline{u} - u)^2 + (\overline{v} - v)^2 + (\overline{w} - w)^2\right) \tag{4}$$

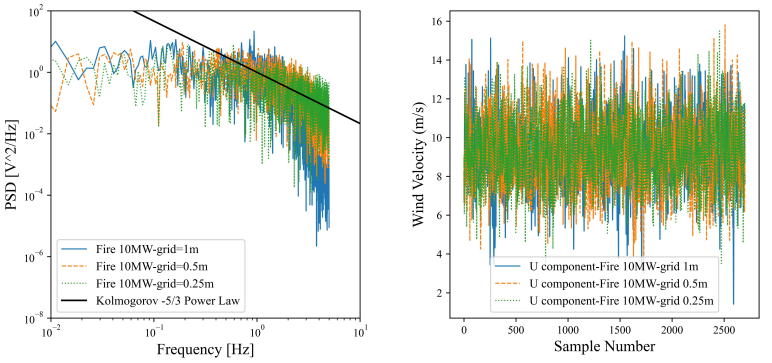

(a) Effect of grid size on PSD distribution(b) Effect of grid size on wind velocity time-series

Figure 4: Effect of grid size and Fire Intensity on Spectral Density of turbulence

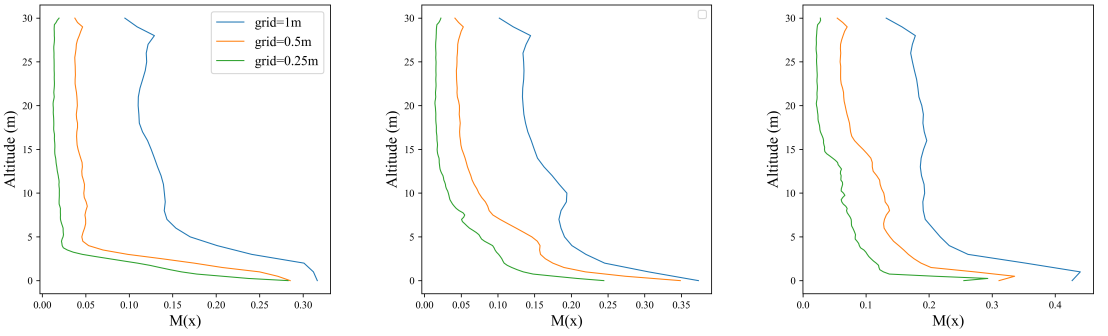

(a) x=0 (fire location) (b) x=10 m downstream of fire (c) x=20 m downstream of fire

Figure 5: Effect of grid size on the measure of turbulence resolution $M(x)$ downstream of a 10 MW fire

and K_{sgs} is the subgrid kinetic energy and is estimated from Deardorff's eddy viscosity model. It is also suggested that a valid Large Eddy Simulation is obtained such that $M(x)<0.2$ [54].

Figure 5 presents the effect of grid size on the turbulence resolution $M(x)$ at different downstream locations of the 10 MW fire. Even though the 0.25 m grid size resolves 90-95% of TKE at most locations, the 0.5 m grid also resolves approximately 80-85% of turbulent kinetic energy except very close to the surface. This indicates that the 0.5 m grid is fine enough for a valid large eddy simulation to capture dominant turbulent structures in our models.

Consequently, the combination of 0.5 m grid size and the *VLES* turbulence model outputs satisfactory results at reasonable computing cost and hence is utilised for the main simulations. It is, acknowledged that the results are grid sensitive to a certain level and a full grid convergence has not been achieved, yet, practical considerations, including the large span of the vegetated area, as well as the need for a considerable height of domain, and large number of simulation scenarios prevent the utilisation of finer grids. The simulation domain is a rectangular block of 600×320×60 m in x, y and z directions, respectively. A burnable area of 200×200 m is defined to provide sufficient space for the formation of a quasi-steady fire propagation, especially for upslope and high wind conditions. To optimise the computational cost, the domain is discretised utilising a non-uniform grid with $0.5 \times 0.5 \times 0.5$ m^3 cells for the vegetated area and its adjacent areas (±4 m) up to 44 m high, moderate cells of $1 \times 1 \times 1$ m^3 for upstream and downstream areas (±30 m), and coarse cells of $2 \times 2 \times 1$ m^3 for the rest of the domain. The defined setup results in a total number of ≈16.7 million cells, parallelised on 32 CPU cores for the duration of the simulation.

3.3. Model architecture and training procedure

This study aims to estimate the spatial distribution of near-surface wind velocity (u_2, v_2, w_2) in the presence of an active grassland fire from the sparsely measured values collected by a UAV swarm at 40 m AGL (u_{40}, v_{40} and w_{40}).

As depicted in Figure 6, the problem is addressed through supervised training of two consecutive CNNs. The first one reconstructs the high-resolution wind and temperature field at 40 m AGL from the sparse or low-resolution input data or measurements. Samples from the high-resolution CFD simulation are used as proxies for UAV measurements. Three swarm sizes (n) are considered, with $n \in \{25, 49, 100\}$. Sampled pixels $P \in \mathbb{R}^{n\times4}$ are then used to generate the low-resolution input matrix $I_{\text{lr}} = \mathcal{F}_{\text{interp, KNN}}(P) \in \mathbb{R}^{13\times13\times4}$ by applying linear interpolation to areas that fall between at least two measurements and assigning the nearest available value (i.e. the nearest neighbour) to outer regions (see Figures 6a and 6b). Additional features including the terrain slope (s), the surface temperature ($T_{\text{surf=2}}$), vegetation type (G_{t}), and vegetation height (H_{g}) are inputted to the model through a dedicated encoder branch concatenated with the corresponding layers of the Super Resolution (SR) model (see Figures 6c and 6d). Hence, the output of the SR model is a high-resolution reconstruction of the wind and temperature field at 40 m AGL:

$$I_{\text{sr}} = \mathcal{F}(I_{\text{lr}}, I_{\text{terrain}}) \tag{5}$$

where $I_{\text{sr}} = (u_{40}, v_{40}, w_{40}, T_{40}) \in \mathbb{R}^{416\times416\times4}$, and $I_{\text{terrain}} = (T_2, s, H_{\text{g}}, G_{\text{t}})$.

The second CNN is trained to map the reconstructed wind and temperature field to near-surface wind fields. Its input matrix includes a concatenation of reconstructed wind and temperature data at 40 m AGL with surface temperature, vegetation height and type, and terrain slope:

$$C = \text{concat}(I_{\text{sr}}, I_{\text{terrain}}) \in \mathbb{R}^{416\times416\times8} \tag{6}$$

while its output is the wind field at 2 m AGL (see Figures 6d and 6e.):

$$I_{\text{surf}} = \mathcal{G}(C), \quad \text{where} \quad I_{\text{surf}} = (u_2, v_2, w_2) \tag{7}$$

The structure for both networks is based on a UNet architecture with residual blocks [64] and includes Convolutional Block Attention Module (CBAM) [65] blocks in both encoder and decoder branches. A sensitivity analysis was conducted to find the optimal number of model parameters, balancing accuracy and training time. Each convolutional layer includes a tanh() activation function, except for the output layer, which uses the linear activation function. It should be noted that the linear activation showed better performance than the Leaky ReLU during initial experiments. Architectural details include zero padding across all convolutional layers, h_{e}–normal kernel initialiser, a kernel size of 3×3 for layers, except for the initial convolutional layer (7×7 kernel) and for the output layer (1×1 kernel). Figure 6 also shows the structure of the encoder and decoder blocks in both models. All blocks include a dropout layer with a dropout ratio of 5% to enhance the model's generalisation and support uncertainty quantification analysis. All models were developed in Python (v3.11) using the TensorFlow library (v2.15) for deep learning model and training. Each model was trained for 200 epochs using the MAE loss function and the Adam optimiser with a batch size of ten, an initial learning rate of 0.0006, and an exponential decay rate of $\beta_1 = 0.9$. Training was performed on an NVIDIA RTX 3080 GPU. Accuracy metrics were monitored after each epoch during the training, and the best models were saved for later use. To evaluate the performance of the neural networks, the mean over N samplings (inference cycles) of the mean absolute error (MAE) and the root mean squared error (RMSE) are calculated as

$$\overline{\text{MAE}}(y, y') = \frac{1}{N}\sum_{k=1}^{N}\frac{1}{n}\left(\sum_{i=1}^{n}|y_i - y'_i|\right) \tag{8}$$

$$\overline{\text{RMSE}}(y, y') = \frac{1}{N}\left(\sum_{k=1}^{N}\sqrt{\frac{1}{n}\left(\sum_{i=1}^{n}\left(y_i - y'_i\right)^2\right)}\right) \tag{9}$$

where y is the ground truth, y' is the estimated value, n is the number of data points per sample (swarm size), and N is the number of samplings (inference cycles).

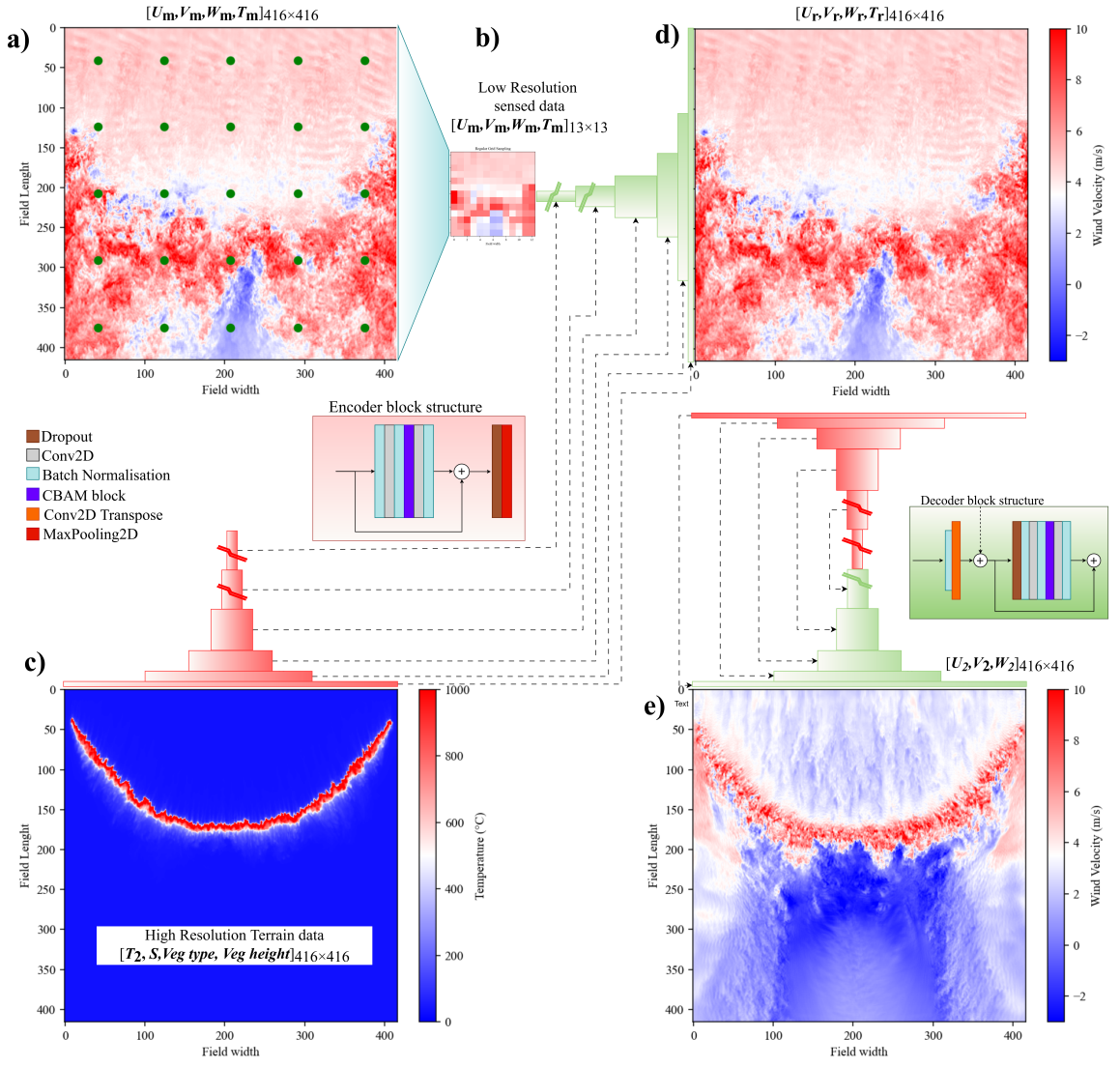

Figure 6: Architecture for reconstructing the high-resolution wind field from low-resolution sensor data, where: (a) high-altitude wind field sampled by UAVs in a structured formation, (b) generated low-resolution wind field used as input to the SR model, (c) terrain and fire data provided as auxiliary inputs, (d) reconstructed high-altitude wind field, and (e) estimated near-surface wind field.

To assess the model's probabilistic performance, three additional metrics are employed: the standard deviation (std), the Prediction Interval Coverage Probability (PICP), and the Prediction Interval Normalised Average Width (PINAW). The standard deviation is a measure of variation or dispersion in a set of data, and can be calculated as

$$\text{std} = \sqrt{\frac{\sum_{k=1}^{N}(x_k - \bar{x})^2}{N-1}} \tag{10}$$

where x_k is the MAE or RMSE of the k^{th} sampling. The PICP evaluates how well a model's Prediction Intervals (PIs) capture the true values. It measures the proportion of true values that actually fall inside their PIs [66]:

$$\text{PICP} = \frac{1}{N}\sum_{k=1}^{N} \epsilon_k \tag{11}$$

Table 3
Effect of the number of model parameters on the SR performance for n=100, utilising first sampling strategy

	model	N.params	U* (m/s)		V* (m/s)		W* (m/s)		T* °C	
			MAE	RMSE	MAE	RMSE	MAE	RMSE	MAE	RMSE
	1	1,030,358	0.744	1.277	0.724	1.241	0.875	1.535	3.860	14.891
Attention	2	3,901,084	0.735	1.268	0.717	1.225	0.867	1.514	3.841	14.632
	3	15,334,136	0.736	1.274	0.720	1.234	0.864	1.510	3.797	14.626
No-Attention	4	3,901,084	0.741	1.283	0.719	1.230	0.869	1.523	3.857	14.814
Att+physics	5	3,901,084	0.737	1.275	0.721	1.235	0.868	1.516	3.845	14.683

* U(m/s) ∈ [-18.7, 55.3], V (m/s)∈ [-38.4, 37.7], W (m/s)∈ [-22.2, 52.1]

$$\epsilon_k = \begin{cases} 1 & \text{if } x_k \in [L_k, U_k] \\ 0 & \text{otherwise} \end{cases} \tag{12}$$

where L_k and U_k are the estimated bounds of the k_{th} PI. The PI Width (PIW) quantifies how uncertain the model is about its prediction for a given input. A larger PICP means that more targets (data points) fall within the PIs, which does not necessarily mean that the model is accurate. The PINAW measures the average PIW normalised by the range of actual observations [66]:

$$\text{PINAW} = \frac{1}{N} \sum_{k=1}^{N} \frac{U_k - L_k}{Y_{\max} - Y_{\min}} \tag{13}$$

where $Y_{\max}$ and $Y_{\min}$ are the maximum and minimum values of the actual observations, respectively. Thus, for a given PICP, a smaller PINAW usually implies a better model.

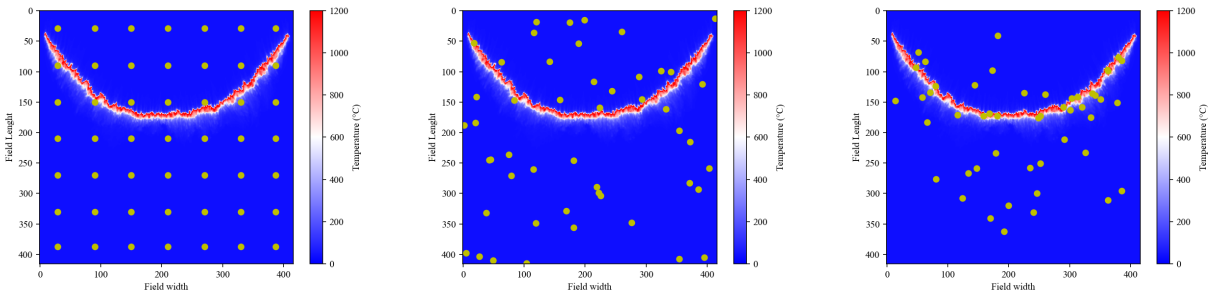

(a) Structured grid sampling (b) Random sampling (c) Temperature-weighted sampling

Figure 7: Domain sampling strategies for low-res input generation

3.4. Dataset

As described before, a total of 150 simulations are conducted with different wind speeds, terrain slopes and vegetation heights and types. The wind and temperature field at 40m and 2m *AGL*– parallel to the terrain–are extracted at different time steps after the ignition and compiled into a dataset for model training. The dataset hence includes 24568 pairs of input-target data, of which 17343 pairs are randomly selected for training, 3652 for validation, and 3573 for the test.

As mentioned earlier (Section 3.3), the low-resolution input data $I_{\text{lr}} \in \mathbb{R}^{13\times13\times4}$ used for training super resolution model are generated from the corresponding high-resolution images through sampling a prescribed number of pixels (25,49,100) and then creating a continuous response surface by performing linear interpolation between measured pixels and assigning nearest neighbour value to outer regions.

To study the effect of sampling distribution on the model performance, three different sampling strategies are examined as depicted in Figure 7:

1. *Strategy I* (Structured Grid Sampling): as shown in Figure 7a, assumes that UAVs are positioned on uniformly spaced locations to provide a regular grid of sampled pixels for the whole duration of the simulation.
2. *Strategy II* (Random Sampling): as shown in Figure 7b, is a purely random sampling of the 416×416 flow field, mimicking mobile UAVs performing uncoordinated measurements or operations.
3. *Strategy III* (Temperature-Weighted Sampling): as shown in Figure 7c, is a particular case of random sampling when the sampling probabilities are biased towards higher temperature regions, mimicking scenarios when UAV swarm has concentrated on the fire front. In this scenario, the probability of a pixel being sampled is defined as follows:

$$P(x, y) = \frac{|T^{0.7}(x, y)|}{\sum_{(i,j)} T(i, j)} \tag{14}$$

where $T(x, y)$ is the temperature at pixel (x, y) and P(x,y) defines the probability of that pixel being sampled. It should be highlighted that the value of 0.7 is selected arbitrarily to balance points sampling over the fire line and across the rest of the domain.

For the first strategy, only one low-resolution image is generated per each high-resolution field, which preserves the 17343, 3652, 3573 split for training, validation and test. In contrast, the second and third strategies produce a different low-resolution field for each sampling iteration, leading to infinitely many possible low-resolution configurations at any specific time. Therefore, a sensitivity analysis is conducted to examine how the number of low-resolution samples per high-resolution field affects the model's generalisability and accuracy. This is, however, discussed in more detail in the next section.

4. Results and Discussion

The proposed models aim to learn the highly complex behaviour and relationship between the measurement-altitude and near-surface wind fields, which is inherently challenging, due to the dynamic and nonlinear nature of the fire–atmosphere interaction. The wind fields are inherently different at measurement height (Z_m=40 m AGL) and the estimation heights (Z_e=2 m AGL). Near-surface wind velocities peak immediately downstream of the flaming front, while the maximum velocities at (Z_m) are observed at a significant distance downstream of the fire location. Additionally, the velocity field near the terrain surface features two counter-rotating wake vortices downstream of the flaming front, increasing the complexity of the flow field.

The models developed in this study are designed to be time-independent, in the sense that they do not use past states of the wind field. Meanwhile, the primary objective is real-time estimation of the near-surface wind field from sparse instantaneous measurements carried out by the UAV swarm. To maintain clarity, this section is divided into two parts. The first part discusses the experiments regarding the evaluation of the super-resolution model for high-altitude wind field reconstruction, and the second part presents the results of the second model trained to estimate the high-resolution near-surface wind field.

4.1. High altitude flow field reconstruction

This section details the accuracy and uncertainty quantification of the models trained for high-altitude wind field reconstruction.

4.1.1. Sensitivity analysis

A comprehensive sensitivity analysis was conducted to evaluate the effect of architectural and training configurations on the accuracy of the super-resolution model. The number of filters in each layer (and consequently the number of trainable parameters) is the first parameter investigated. As presented in Table 3, increasing the number of trainable parameters from 1M to 4M improved the model performance. However, further increasing the model size has resulted in a decline in the model's accuracy, most likely due to overfitting or vanishing gradients. Comparing Model 2 and Model 4 highlights the impact of incorporating the Convolutional Block Attention Module (CBAM) blocks, which have improved the accuracy of the model outputs. To integrate physical constraints into the model training process, a

Table 4
Effect of the number of UAVs on the SR performance utilising first sampling strategy

N. UAV	U* (m/s)		V* (m/s)		W* (m/s)		T* C	
	MAE	RMSE	MAE	RMSE	MAE	RMSE	MAE	RMSE
25 (5*5)	0.767	1.341	0.745	1.285	0.896	1.589	4.295	16.278
49 (7*7)	0.755	1.315	0.735	1.265	0.882	1.558	4.091	15.613
100 (10*10)	0.735	1.268	0.717	1.225	0.867	1.514	3.841	14.632

* U(m/s) ∈ [-18.7, 55.3], V (m/s)∈ [-38.4, 37.7], W (m/s)∈ [-22.2, 52.1]

Table 5
Effect of increasing the number of randomly sampled low-resolution inputs per high-resolution field on the accuracy of the super-resolution (SR) model. The second strategy with n=100 UAVs is used in all cases.

N. input samples	U* (m/s)		V* (m/s)		W* (m/s)		T* C	
	MAE	RMSE	MAE	RMSE	MAE	RMSE	MAE	RMSE
2	0.752	1.313	0.726	1.248	0.880	1.558	4.131	15.669
3	0.748	1.306	0.722	1.243	0.877	1.549	4.082	15.614
5	0.732	1.274	0.717	1.236	0.868	1.539	3.995	15.557

* U(m/s) ∈ [-18.7, 55.3], V (m/s)∈ [-38.4, 37.7], W (m/s)∈ [-22.2, 52.1]

physics-constrained version of the model is implemented by incorporating the incompressible version of the continuity equation into the loss functions as follows:

$$Loss_{\text{total}} = Loss_{\text{residual}} + |\nabla \cdot \vec{V}|$$

Where $Loss_{\text{total}}$ is the final loss utilised to train the model. However, despite increasing the complexity and training time, utilising this constraint did not enhance model performance as indicated in table 3. Based on this analysis, the second model architecture with 4M trainable parameters is adopted as the optimal architecture for the subsequent examinations.

The second part examines the effect of the number of UAVs (sampling points) on the accuracy of the super-resolution model. As previously mentioned, three different sizes of the UAV swarm with 25, 49, and 100 UAVs were tested for generating low-resolution inputs utilising the first sampling strategy. Three distinct models were hence trained and tested. Table 4 presents the corresponding accuracy metrics for these models. It is indicated that increasing the number of UAVs–as expected– results in improvement in wind field reconstruction accuracy. Though it should be highlighted that the observed performance improvement is relatively small, with the difference between MAE values remaining within 4% for velocity components and 10% for temperature, despite changing swarm size from 25 to 100, a 4x increase.

The final examination investigates how training models with various low-resolution representations of a single high-resolution flow field affects model performance. Accordingly, three different models were trained utilising 2, 3 and 5 low-resolution input representations per high-resolution wind field as presented in Table 5. Considering that each low-resolution sample should be treated as a distinct input along with its corresponding high-resolution target, it effectively multiplies the dataset size and consequently, the training time. Obtained results indicated that while increasing the number of low-resolution inputs slightly increases model performance and generalisability, it comes at the cost of a proportional increase in training time. This would hence make it impractical to account for a high number of inputs for training on the full dataset.

4.1.2. Performance evaluation

The primary model is trained so as to ensure accurate super-resolution estimations regardless of the sampling strategy or swarm size and distribution. Hence, the training dataset consists of low-resolution and high-resolution pairs generated using all three sampling strategies and varying swarm sizes. Considering 1 low-resolution representation per high-resolution field for the first sampling strategy and **3** for the second and third sampling strategies, the training dataset would include 18×17325 input-output pairs of data, excluding the case with the third sampling strategy and n=49 out for testing the model. This model was trained for 100 epochs due to the substantial computational cost and the observed lack of improvement after 40 epochs.

Table 6
Performance evaluation metrics and their standard deviation for the SR model trained on the full dataset

N. UAV	U (m/s)		V (m/s)		W (m/s)		T	
(strategy)	MAE (std)	RMSE (std)	MAE (std)	RMSE (std)	MAE (std)	RMSE (std)	MAE (std)	RMSE (std)
25 (1)	0.755	1.315	0.731	1.261	0.883	1.562	4.158	15.984
49 (1)	0.752	1.308	0.730	1.259	0.881	1.555	4.111	15.787
100 (1)	0.748	1.301	0.729	1.257	0.878	1.546	4.052	15.570
25 (2)	0.762	1.325	0.732	1.263	0.884	1.565	4.189	16.060
49 (2)	0.756	1.314	0.731	1.261	0.882	1.559	4.145	15.915
100 (2)	0.752	1.307	0.730	1.259	0.880	1.552	4.097	15.729
25 (3)	0.759	1.321	0.732	1.264	0.884	1.566	4.189	16.122
100 (3)	0.755	1.315	0.732	1.263	0.883	1.563	4.164	16.045
Overall	**0.755 (0.0101)**	**1.313 (0.0177)**	**0.731 (0.088)**	**1.261 (0.0153)**	**0.882 (0.0108)**	**1.558 (0.0198)**	**4.138 (0.0736)**	**15.901 (0.2618)**

* U(m/s) ∈ [-18.7, 55.3], V (m/s)∈ [-38.4, 37.7], W (m/s)∈ [-22.2, 52.1]

The model accuracy is evaluated utilising the MAE and RMSE, while the uncertainty of estimations is quantified utilising Std of these metrics. For each testing subset, the model undergoes 15 inference cycles with randomly selected low-resolution batches to accompany each sample. Table 6 presents the average performance metrics along with the overall standard deviation of these metrics, evaluated against the testing sets of the low-resolution datasets used to train the model, and then averaged. It should, however, be highlighted that a fixed test set is used per scenario across all inference cycles to solely focus on the model uncertainty and the data uncertainty does not affect the evaluations.

Overall, the model achieved an MAE and RMSE of 0.755, 1.313 (m/s), respectively, for the U, 0.731 and 1.261 for the V, and 0.882 and 1.558 for the W component of velocity. For the temperature (T), these values were equal to 4.138 and 15.901. Comparing these values to their value ranges, it could be concluded that the model achieves acceptable accuracy across all predicted variables. Furthermore, the standard deviation of all metrics remains within 1.5% of their respective averages, indicating a low uncertainty of model estimations within the training range of data.

Concerning the influence of the sampling strategy on the model performance, while the first strategy yields slightly lower MAE and RMSE values, the differences across all three strategies were negligible, suggesting a proper model generalisation. In addition, increasing the number of UAVs from 25 to 100 also proved to have a negligible effect on the model accuracy improvement.

Figure 8 presents a visual comparison between the target and mean predictions of the SR model for the case with $u_{10} = 4m/s$, H_g=0.2 m, and horizontal terrain (S=0 %). The low-resolution samples were generated assuming a swarm size of n=100 UAVs, utilising the third sampling strategy (100(3)). The columns of the figure present the ground truth (first column), the model's mean predictions (second column), and the error values (third column). The final column compares interpolated input, ground truth, and predicted values along the domain's centerline. Each row corresponds to one parameter including U (Figure 8a), V (Figure 8b), and W (Figure 8c) components of velocity, and temperature (T) (Figure 8d).

It could be observed that while the model prediction is a smoothed version of the true field, the model captures the general pattern of the wind field within the fire plume and the surrounding area and provides an accurate estimation of the upstream wind field, which is a significant improvement over simple interpolation. The narrow uncertainty bounds further validate the model's reliability in this context.

4.1.3. Uncertainty quantification

The uncertainty of estimations could arise from both model limitations (epistemic) and data variability (aleatoric). While these uncertainty sources could be separately evaluated, such isolation provides limited added value in operational contexts. This section hence evaluates model behaviour under realistic operational variability, including variations in the spatial distribution of UAVs and sensor-level measurement noise, which together reflect real-world deployment scenarios.

Wind measurement using UAVs is inherently noisy, leading to high levels of uncertainty. Additionally, the number of UAVs in real-world scenarios is often lower than that in controlled simulations. Therefore, the trained model is evaluated against unseen swarm sizes, varying spatial distributions, and different input noise levels. Each high-resolution wind field within the test set is randomly sampled multiple times–with different random seeds from training cycles– to generate several Low-resolution representations of the same high-resolution wind field, replicating the infinitely possible spatial distribution of UAVs over the domain. These versions are then used to make multiple

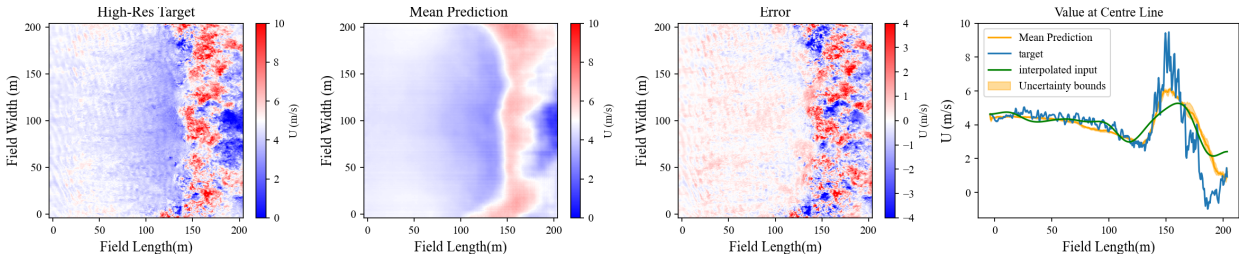

(a) Reconstruction results for U (m/s) component of velocity

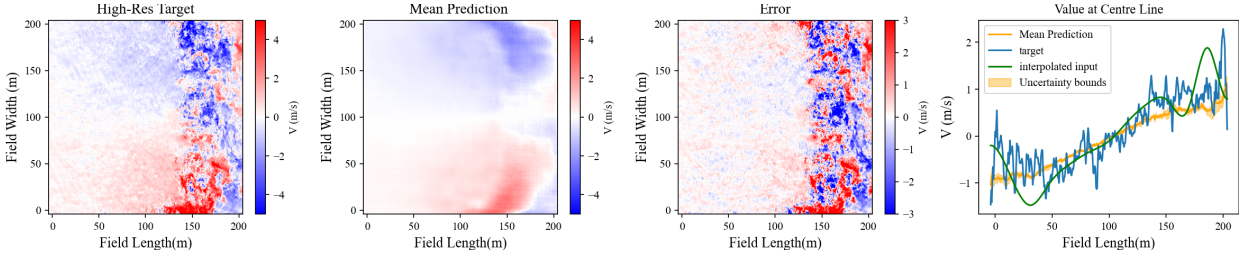

(b) Reconstruction results for V (m/s) component of velocity

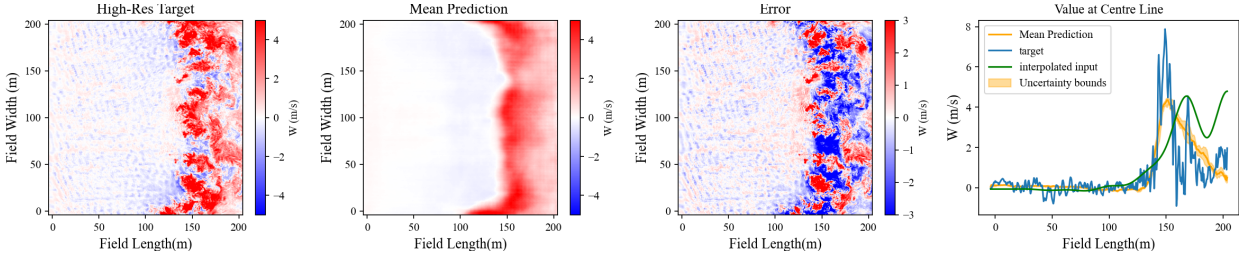

(c) Reconstruction results for W (m/s) component of velocity

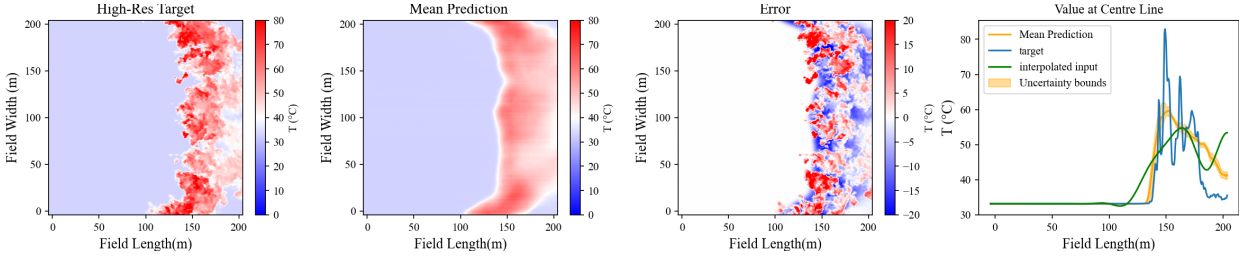

(d) Reconstruction results for temperature T °C

Figure 8: Results of the high-resolution wind and temperature field reconstruction for case 100(3) $u_{10} = 4$ m/s, $H_g = 0.2$ m and $S = 0\%$, depicting the high-resolution ground truth/target, mean prediction of the model, the reconstruction error, and comparison of the reconstructed value at the centre line of the field with model estimation and the model input.

estimations of the same high-resolution field, capturing the combined effect of model uncertainty and sampling variability.

Table 7 presents the accuracy and uncertainty metrics across unseen cases of swarm size and sampling representations. The first investigation quantifies the effect of decreasing the swarm size from 49 to 16 and then to 9, utilising third sampling strategies. It is indicated that despite the model was not trained on data from 49(3), it provides comparably accurate estimations (i.e., MAE = 0.755 and an RMSE = 1.314 for U) as those seen during the training. Further reducing the swarm size to 16 and then 9 leads to a slight increase of MAE of U from 0.755 to 0.762 and then to 0.777, respectively, corresponding to a 3% increase, indicating the model's resilience to lower-resolution inputs. The model uncertainty is then quantified in terms of Prediction Interval Coverage Probability (PICP), and the Prediction Interval Normalised Average Width (PINAW), due to the minimal variations of the MAE and RMSE standard deviations across different cases, making it difficult to identify trends or draw conclusions. The PICP for the U component increases from

Table 7
Evaluation of performance metrics and uncertainty of the SR model against unseen UAV numbers

		N. UAVs (sampling strategy)				
		49 (3)	16 (3)	9 (3)	9 (2)	9 (1)
U	**MAE**	**0.755**	**0.762**	**0.777**	**0.786**	**0.767**
	RMSE	1.314	1.327	1.347	1.359	1.333
	PICP	0.107	0.123	0.142	0.144	0.134
	PINAW (%)	**0.485**	**0.568**	**0.688**	**0.719**	**0.661**
V	**MAE**	**0.732**	**0.733**	**0.734**	**0.734**	**0.733**
	RMSE	1.262	1.265	1.266	1.266	1.265
	PICP	0.057	0.059	0.061	0.063	0.060
	PINAW(%)	**0.168**	**0.176**	**0.184**	**0.192**	**0.182**
W	**MAE**	**0.884**	**0.885**	**0.887**	**0.887**	**0.886**
	RMSE	1.564	1.569	1.572	1.571	1.570
	PICP	0.058	0.060	0.063	0.065	0.064
	PINAW(%)	**0.250**	**0.257**	**0.269**	**0.283**	**0.265**
T	**MAE**	**4.168**	**4.207**	**4.247**	**4.261**	**4.222**
	RMSE	16.052	16.185	16.274	16.211	16.198
	PICP	0.188	0.194	0.202	0.200	0.191
	PINAW(%)	**0.185**	**0.194**	**0.211**	**0.230**	**0.212**

Table 8
Evaluation of performance metrics and uncertainty of the SR model against different measurement noise

		N. UAVs (sampling strategy)								
		9(2)				25(3)	49(3)			
	noise level	no noise	10%	30%	50%	50%	no noise	10%	30%	50%
U	**MAE**	**0.786**	**0.936**	**1.513**	**2.038**	**1.736**	**0.755**	**0.790**	**1.143**	**1.579**
	RMSE	1.359	1.530	2.138	2.730	2.369	1.314	1.358	1.743	2.190
	PICP	0.144	0.259	0.494	0.512	0.451	0.107	0.168	0.394	0.430
	PINAW(%)	**0.719**	**1.462**	**3.765**	**5.121**	**4.006**	**0.485**	**0.865**	**2.533**	**3.516**
V	**MAE**	**0.734**	**0.736**	**0.750**	**0.766**	**0.757**	**0.732**	**0.733**	**0.738**	**0.750**
	RMSE	1.266	1.270	1.293	1.321	1.304	1.262	1.264	1.273	1.280
	PICP	0.063	0.073	0.110	0.132	0.112	0.057	0.062	0.088	0.103
	PINAW(%)	**0.192**	**0.228**	**0.363**	**0.456**	**0.378**	**0.168**	**0.187**	**0.271**	**0.336**
W	**MAE**	**0.887**	**0.890**	**0.911**	**0.935**	**0.921**	**0.884**	**0.884**	**0.894**	**0.912**
	RMSE	1.571	1.579	1.628	1.676	1.650	1.564	1.566	1.588	1.628
	PICP	0.065	0.075	0.111	0.134	0.115	0.058	0.064	0.091	0.107
	PINAW(%)	**0.283**	**0.335**	**0.524**	**0.656**	**0.553**	**0.251**	**0.278**	**0.404**	**0.501**
T	**MAE**	**4.261**	**4.501**	**5.263**	**5.937**	**5.523**	**4.168**	**4.233**	**4.714**	**5.292**
	RMSE	16.211	16.381	17.016	17.624	17.274	16.052	16.094	16.418	16.913
	PICP	0.200	0.266	0.431	0.440	0.376	0.188	0.207	0.356	0.351
	PINAW(%)	**0.230**	**0.327**	**0.621**	**0.818**	**0.666**	**0.185**	**0.242**	**0.444**	**0.595**

0.107 to 0.142 while decreasing the swarm size from case 49 to 9, while PINAW increases from 0.485% to 0.688%, equivalent to 42% increase. This suggests that improved PICP coverage in cases with smaller UAV numbers primarily corresponds to the expanded width of PIs, reflecting better PICP coverage of values at the cost of higher uncertainty of the model. This trend is more pronounced in the U and T parameters. For T, the MAE increases from 4.168 to 4.247 (≈1.9%) while PINAW increases by ≈14%. However, for V and W components, MAE and RMSE values exhibit small changes of ≈0.2% while PINAW rises less than ≈8%.

Comparing different sampling strategies with the same swarm size of n=9, it is indicated that while performance variations are minimal across different sampling strategies (MAE for U ranges from 0.767 to 0.786), the PICP and PINAW vary up to ≈9%, with the second sampling strategy exhibiting both higher accuracy and higher uncertainty. In summary, the model maintains a satisfactory performance under a reduced number of UAVs to 9, with a marginal accuracy degradation; however, the model's uncertainty increases as a result. More importantly, the model

demonstrates robustness against sampling strategies, indicating that the system can function without the need for a dedicated subset of UAVs to remain stationary for persistent wind measurement. This highlights the system's flexibility for deployment in dynamic UAV operations.

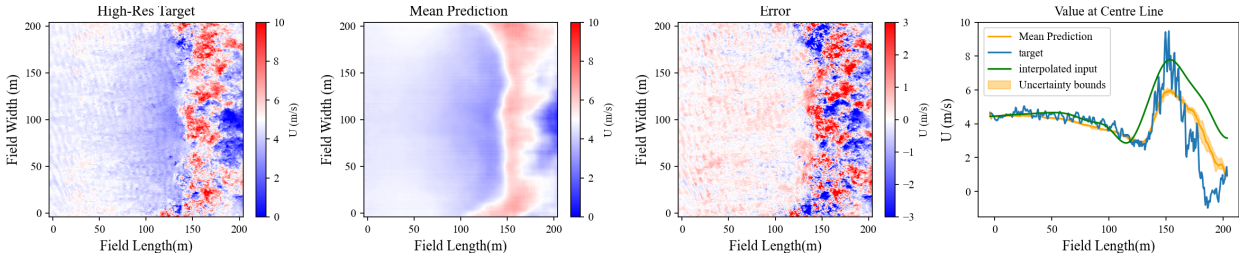

(a) Measurement noise= 0%

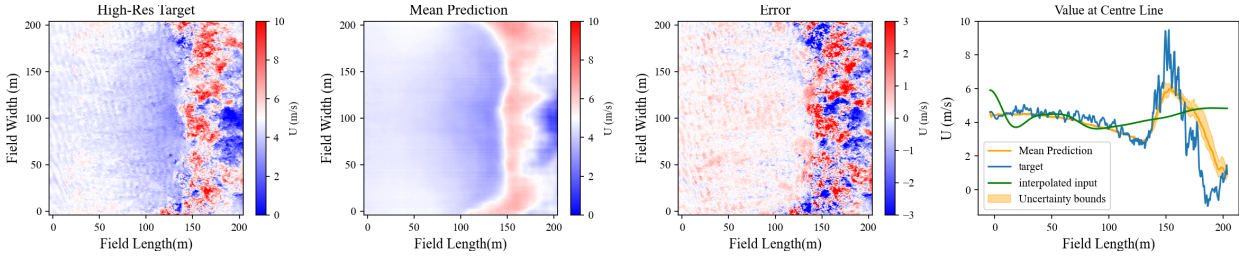

(b) Measurement noise= 10%

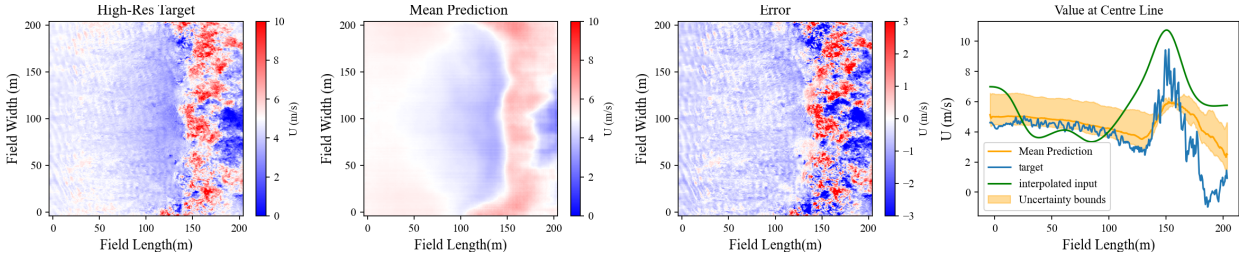

(c) Measurement noise= 30%

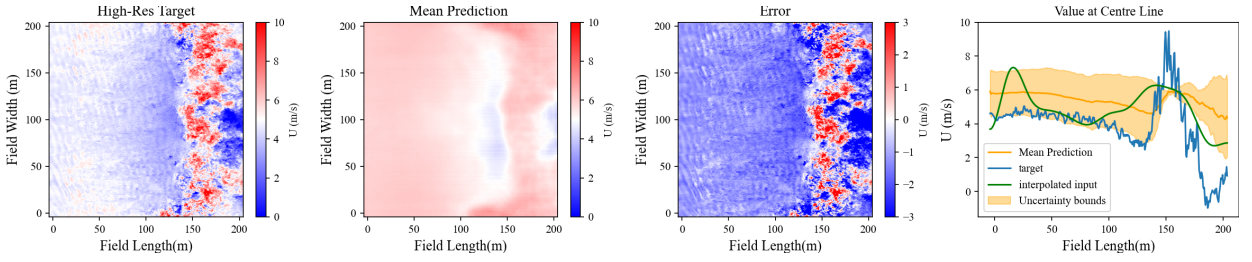

(d) Measurement noise= 50%

Figure 9: Results of the high-altitude reconstruction of the U-component for case 49(3), $u_{10} = 4$ m/s, $H_g = 0.2$ m and $S = 0\%$ under different measurement noise levels, depicting the high-resolution ground truth/target, mean prediction of the model, the reconstruction error, and comparison of the reconstructed value at the centre line of the field with model estimation and the model input.

Table 8 presents the performance and uncertainty metrics under different input noise levels of 10%, 30% and 50%, for different swarm sizes of n from 9 to 49, utilising the third sampling strategy. The model performance is evaluated using multiple low-resolution representations subjected to random Gaussian noise. This approach effectively simulates a realistic scenario subject to sensor, environmental and swarm distribution uncertainties. The input Gaussian noise (N) is defined proportional to the standard deviation of each component and each input batch, which results in the noisy input data in the form of $U_{Noisy} = N \times U + U$. The noisy data is then used to generate low-resolution input images.

Table 9
performance evaluation metrics and uncertainty of the NSR model against different testing subsets

	U (m/s)		V (m/s)		W (m/s)	
UAV number (strategy)	MAE (std)	RMSE (std)	MAE (std)	RMSE (std)	MAE (std)	RMSE (std)
25 (1)	0.862	1.337	0.679	1.142	0.552	1.011
49 (1)	0.859	1.335	0.677	1.14	0.551	1.01
100 (1)	0.857	1.331	0.676	1.138	0.551	1.01
25 (2)	0.867	1.345	0.679	1.142	0.552	1.01
49 (2)	0.862	1.337	0.678	1.141	0.552	1.01
100 (2)	0.859	1.334	0.677	1.139	0.551	1.01
25 (3)	0.867	1.344	0.68	1.144	0.552	1.011
100 (3)	0.864	1.341	0.679	1.142	0.551	1.01
Overall	0.849 (0.040)	1.323 (0.046)	0.672 (0.017)	1.022 (0.023)	0.551 (0.002)	1.010 (0.002)

* U(m/s) ∈ [-26.1, 41.3], V (m/s)∈ [-33.1, 27.35], W (m/s)∈ [-25.6, 29.95]

The obtained results indicate that generally, increasing the noise level reduces the model accuracy and increases predictive uncertainty. For instance, with a swarm made of 9 UAVs, introducing only 10% measurement noise raises the MAE for U from 0.786 to 0.936 (≈19%), and RMSE from 1.359 to 1.530 (≈12%), while PINAW increases from 0.719% to 1.462% and PICP from 0.144 to 0.259. For temperature, MAE increases moderately (≈6%), and PINAW rises from 0.230% to 0.327%. This is, however, less significant in V and W components with MAE rising from 0.192 to 0.228% for the V, and from 0.283 to 0.335% for W, and from 0.230 to 0.327% for temperature (T). Increasing the noise ratio to 50%, the MAE increases from 0.786 to 2.038 (≈160%), and PINAW from 0.719% to 5.121% of the data range for U. For temperature, the MAE rises by ≈40% and PINAW from 0.23% to 0.818%, all relatively low compared with the data ranges. Additionally, it is found that increasing the swarm size improves the model accuracy and reduces the model uncertainty, particularly under high measurement noise conditions–an interesting finding. For example, under 50% noise condition, increasing the swarm size from 9 to 25 leads to a reduction of the MAE and PINAW values for U from 2.038 to 1.736 and from 5.121 to 4.006, respectively. This corresponds to a 15% and 22% reduction in MAE and PINAW values, respectively.

Figure 9 presents a graphical representation of the super-resolution reconstruction of the velocity and temperature components, under different measurement noise levels in a case with 49 UAVs, utilising the third sampling strategy. It is indicated that the spatial accuracy of reconstruction reduces, and the PIs widen as the input noise increases. Notably, by increasing the input noise level, the average estimations of the velocity tend to overestimate the wind velocity at regions behind the fire plume for $u_{10} \leqslant 6$ m/s and underestimation for $u_{10} > 6$, and a smoother and more uniform estimation of the wind field ahead of the fire, suggesting convergence towards a mean flow field. However, the model consistently underpredicts temperature values within the plume across varying noise levels (see Figure 12). Additionally, Values behind the fire plume remain largely stable, and prediction variations remain within ±0.5 °C.

4.2. Near surface wind field reconstruction

This section presents the performance and uncertainty quantifications of the model trained to reconstruct or estimate the near-surface wind field $I_{\text{surf}} = (u_2, v_2, w_2) \in \mathbb{R}^{416\times416\times3}$, from a concatenation of reconstructed high altitude wind field–from previous section– with the high-resolution data corresponding to the surface temperature, vegetation height and type, and the terrain slope $C = concat(I_{sr}, I_{\text{terrain}}) \in \mathbb{R}^{416\times416\times8}$. The model is referred to as *NSR* from here on, short for the near-surface reconstruction model.

The training configurations, including the model architecture, number of trainable parameters, activation functions, and kernel sizes, of the NSR are kept similar to the SR model in the previous section. The training dataset is formed by pairing the reconstructed outputs of the SR model as the input and the high-resolution near-surface wind field as the target. Considering that the uncertain estimations of the first model are used to generate uncertain near-surface wind field estimations in the second model, the NSR model indirectly inherits and propagates this uncertainty, resulting in a cumulative uncertainty effect across the two-stage framework.

To balance probabilistic performance requirements with training costs, 3 different high-resolution representations of the high-altitude wind field are generated by the SR model and used as input to train the NSR model, forming a data set with 24 × 17325 input-output pairs of data, leaving the case with third sampling strategy and n=49 out for testing the model.

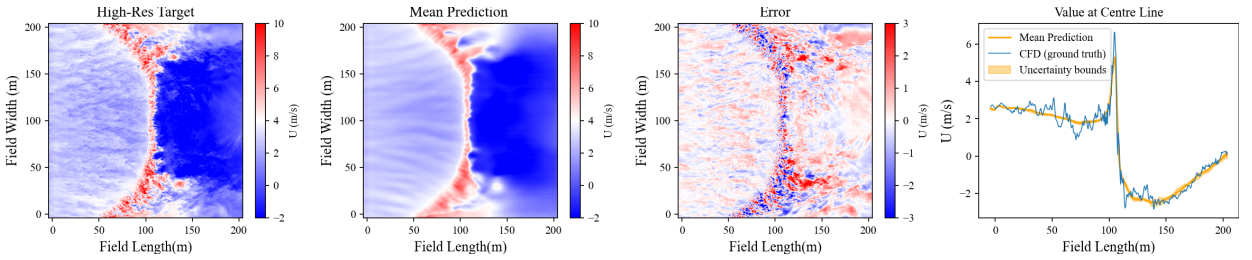

(a) Estimation results for U (m/s) component of velocity

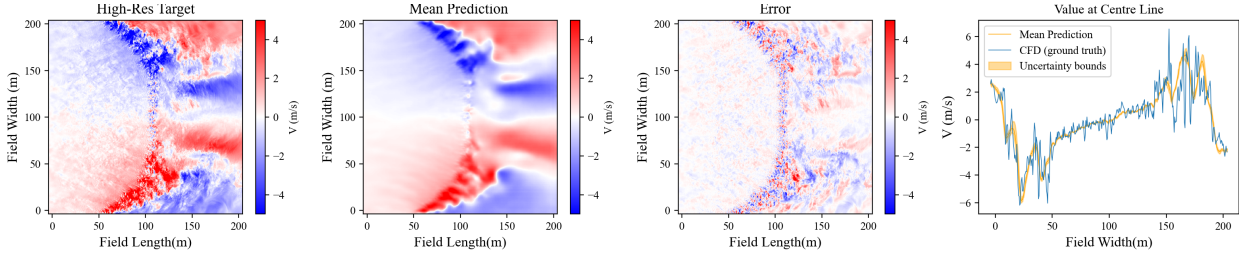

(b) Estimation results for V (m/s) component of velocity

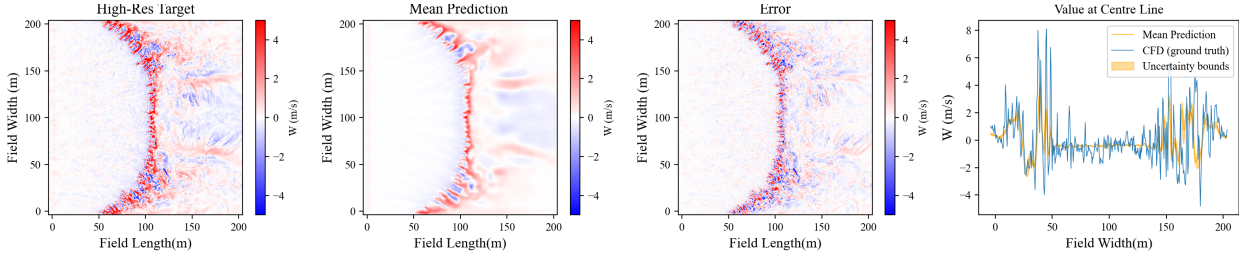

(c) Estimation results for W (m/s) component of velocity

Figure 10: Results of the high-resolution near-surface wind field reconstruction for case 49(3), and environmental conditions of $u_{10} = 4$ m/s, $H_g = 0.2$ m and $S = 0\%$.

4.2.1. Performance evaluation

Similar to the previous section, the effect of embedding the attention mechanism in the model on the estimation accuracy is studied. The fully convolutional baseline exhibited a promising performance with MAE=0.785 and RMSE =1.255 for U, MAE=0.656 and RMSE =1.123 for V, and MAE=0.555 and RMSE =1.021 for W component of velocity, which are, however, up to 5.5% higher than corresponding values achieved by the attention-based model presented in Table 9. It is also worth mentioning that the fully convolutional model tend to provide a smoother representation of the wind field compared to the attention-based model. Consequently, the attention mechanism is embedded into the final model.

Table 9 presents the average performance metrics of the NSR model testing subsets of the reconstructed wind fields used to train the model. Similar to the section 4.1.2, the model has undergone multiple inference cycles for each testing subset with randomly sampled batches to accompany each sample.

Overall, the model achieved MAE and RMSE values of 0.849 and 1.323 for U, 0.672 and 1.142 for V, and 0.551 and 1.01 for the W component of velocity, respectively. Additionally, the standard deviation of all metrics is bound in a range of 5% of their means, indicating relatively high confidence in model estimations and low epistemic uncertainty. Besides, the overall impact of the high-altitude sampling strategy proved to be negligible, as indicated by the minor variation in MAE and RMSE metrics across different scenarios. Also, increasing the number of UAVs within the swarm from 25 to 100 exhibited a negligible effect of less than 1% on the average accuracy of the model across different sampling scenarios, thus it could be considered negligible.

Figure 10 presents a visual representation of the the NSR model estimations for the case with $u_{10} = 4, \text{m/s}$, $H_g = 0.2, \text{m}$, and flat terrain ($S = 0\%$), at the same time instance of the previous figures. The near-surface wind is estimated utilising the reconstructed high-altitude wind field from the scenario with 49 UAVs utilising the

Table 10
Evaluation of performance metrics and uncertainty of the NSR model against unseen Swarm sizes

		N. UAVs (sampling strategy)				
		49 (3)	16 (3)	9 (3)	9 (2)	9 (1)
U (m/s)	**MAE**	**0.861**	**0.873**	**0.880**	**0.884**	**0.873**
	RMSE	1.337	1.352	1.362	1.367	1.353
	PICP	0.0597	0.0653	0.0708	0.0725	0.0689
	PINAW (%)	**0.6410**	**0.7210**	**0.7960**	**0.8270**	**0.783**
V (m/s)	**MAE**	**0.679**	**0.681**	**0.685**	**0.683**	**0.682**
	RMSE	1.142	1.146	1.151	1.149	1.146
	PICP	0.075	0.078	0.080	0.081	0.07920
	PINAW (%)	**0.449**	**0.472**	**0.489**	**0.502**	**0.48300**
W(m/s)	**MAE**	**0.552**	**0.552**	**0.553**	**0.552**	**0.552**
	RMSE	1.011	1.011	1.012	1.011	1.011
	PICP	0.047	0.048	0.049	0.049	0.049
	PINAW (%)	**0.2710**	**0.2770**	**0.2830**	**0.2860**	**0.2830**

Table 11
Evaluation of performance metrics and uncertainty of the NSR model against different measurement noise

		N. UAVs (sampling strategy)									
		9(2)				25(3)		49(3)			
	Noise level	0 %	10%	30%	50%	0 %	50%	0 %	10%	30%	50%
U (m/s)	**MAE**	**0.884**	**0.965**	**1.123**	**1.490**	**0.867**	**1.358**	**0.861**	**0.893**	**1.057**	**1.267**
	RMSE	1.367	1.460	1.742	2.073	1.344	1.875	1.337	1.374	1.544	1.766
	PICP	0.073	0.107	0.187	0.205	0.063	0.179	0.060	0.074	0.148	0.166
	PINAW (%)	**0.827**	**1.283**	**2.642**	**3.479**	**0.687**	**2.734**	**0.641**	**0.837**	**1.798**	**2.384**
V (m/s)	**MAE**	**0.683**	**0.690**	**0.710**	**0.761**	**0.68**	**0.748**	**0.679**	**0.681**	**0.702**	**0.735**
	RMSE	1.149	1.157	1.197	1.255	1.144	1.235	1.142	1.145	1.171	1.213
	PICP	0.081	0.096	0.137	0.156	0.0768	0.139	0.075	0.081	0.114	0.130
	PINAW (%)	**0.5020**	**0.585**	**0.862**	**1.026**	**0.461**	**0.901**	**0.4490**	**0.488**	**0.693**	**0.831**
W(m/s)	**MAE**	**0.552**	**0.554**	**0.558**	**0.565**	**0.552**	**0.563**	**0.552**	**0.552**	**0.556**	**0.561**
	RMSE	1.011	1.012	1.016	1.022	1.011	1.019	1.011	1.011	1.014	1.017
	PICP	0.049	0.057	0.078	0.088	0.0475	0.078	0.047	0.050	0.066	0.073
	PINAW (%)	**0.286**	**0.316**	**0.401**	**0.451**	0.275	**0.414**	**0.271**	**0.286**	**0.351**	**0.392**

third sampling strategy (49(3)). Overall, the NSR model demonstrated satisfactory performance while mapping the instantaneous 40 m AGL wind field to its near-surface counterpart.

The estimations for the U component-as depicted in Figures 10a, 15a, and 18a- indicate that the model accurately captures the structure of the fire-induced wind field, including the acceleration zone above the flaming front and the downstream vortex zone. Similarly, the estimations of V component -as depicted in Figure 10b, 16a, and 19a- show that the model reproduces the turbulent structure of the fire-induced wind accurately. However, the W component is highly oscillatory -as depicted in 10c, 17a, and 20a-, which leads to higher estimation errors specifically within the downstream vortex region. As a general observation, the model underestimates extreme velocity values, particularly near the flaming front, up to 24% for U and up to 60% for the W component. This, however, is not surprising as the model is trained to estimate the average and large-scale behaviour of the flow rather than the oscillatory and vortical structure of the wind field at small scales, which justifies this limitation.

4.2.2. Uncertainty quantification

This section examines the combined effect of data measurement uncertainty, including the spatial distribution of sampling points and the measurement device errors, and epistemic uncertainty on model performance and estimation reliability. As discussed in Section 4.1.3, multiple low-resolution versions were generated for each high-resolution wind field at flying altitude, which were then used to reconstruct the high-altitude wind field and perform uncertainty analysis. Subsequently, these reconstructed high-altitude wind fields are used in this section to generate multiple estimations of the near-surface wind field, providing both mean values and uncertainty measures. Consequently, the

uncertainty propagates throughout the entire modelling pipeline, as the uncertain estimations of the first model inform the uncertainty in the second model, thereby allowing for an assessment of the total uncertainty of the developed framework.

Table 10 presents the accuracy and uncertainty metrics of the NSR model across unseen combinations of the swarm size and sampling strategies. The obtained results indicate that the model is generally robust to changes in the swarm size. For example, reducing the number of UAVs from 49 to 9 led to a slight increase in the MAE, corresponding to an approximate rise of 2.5% from 0.86 to 0.88 for the U. The RMSE metric also shows a similar trend. However, the uncertainty metric, PINAW, grows from 0.6410 to 0.7960 as UAV numbers decrease, indicating a slightly broader interval for predictions. However, the model indicates consistency in terms of accuracy metrics and uncertainty measures for the V and W components of velocity, regardless of the number of UAVs. As a result, it can be concluded that the model maintains high accuracy across various UAV configurations with a slight increase in uncertainty for reduced sizes of the swarm.

Table 11 presents the performance of the NSR model under different levels of input measurement noise. Similar to the UAV distribution and swarm size, the uncertainty caused by measurement noise propagates throughout the entire modelling pipeline and affects the NSR predictions. As expected, increased measurement noise leads to decreased estimation accuracy and increased uncertainty, particularly for smaller swarm sizes. For example, increasing the input noise to 50% leads to a rise in MAE from 0.884 to 1.49 for case 9(2), corresponding to 69% increase, which demonstrates a clear sensitivity to input noise. As noise increases, RMSE values also rise significantly, indicating larger discrepancies between predicted and true values. Both PICP and PINAW measures increase by increasing the input noise, particularly for case 9(2), where PICP for U increases from 0.073 to 0.205 (≈180%) and PINAW rises from 0.827 to 3.479 (≈320%). Considering the effect of swarm size, it could be concluded that increasing the number of UAVs, enhances the model robustness against input noise, as evidenced by the lower MAE, RMSE, PICP, and PINAW values for U in case 49(3) compared to 25(3) and 9(2). Regarding the V and W components of velocity, it could be highlighted that while uncertainty generally increases with noise -for example, PINAW values change from 0.502 to 1.026 for V and from 0.286 to 0.316 for W in case 9(2)-, this increase is less dramatic compared to the U component. This is, however, partly because, despite their broad range, a significant portion of the V and especially W component values are near or equal to zero. In such cases, the uncertainty has little impact on the estimations, resulting in lower average uncertainty metrics. Even as the uncertainty increases in regions with non-zero values, the overall average remains small.

Figure 11 presents the estimated U component of the near-surface wind field for case 49(3), $u_{10} = 4$ m/s, $H_g = 0.2$ m and $S = 0\%$, under increased measurement noise levels. Additional examples are presented in Figure 15 and 18 U, Figure 13, 16, and 19 for V, and Figure 14, 17, and 20 for W component of velocity. It can generally be observed that although the model produces a satisfactorily smoothed version of the wind field, the quality of predictions declines as input noise increases. This is reflected as the widened prediction intervals (PIs), which correspond to the higher levels of input noise. These observations underline the model's sensitivity to input quality and reiterate the importance of accurate measurements for reliable wind field estimation.

5. Model Generalisation and Limitations

This section briefly addresses the practical capabilities and current limitations of the proposed method. As noted, the model was trained and tested on a square terrain with a constant slope, simulating a line fire ignited at the centre of the upstream boundary. But how applicable is this method to a large-scale wildfire? We believe that this method could be generalised by adopting a patching technique, where the desired area or firefront is divided into a series of square patches and the wind field is estimated for each patch independently. Within each patch, the fire could be considered a line fire, making the proposed framework feasible for use in larger wildfires.

However, the model in its current form has a series of limitations. First, the terrain is unlikely to remain constant and uniform within a 200×200 m^2 area. Besides, the assumption of a symmetric line fire across all patches seems to be unrealistic, as fire fronts can vary significantly in shape within each patch. Another important limitation is that the model is trained with input wind directed along the field length, meaning that patches must be aligned parallel to the ambient wind, which would be extremely difficult to achieve in actual fires and complex terrains. Finally, the model assumes that all data is collected at a constant height, directly parallel to the terrain, which may be difficult to obtain in actual fire conditions.

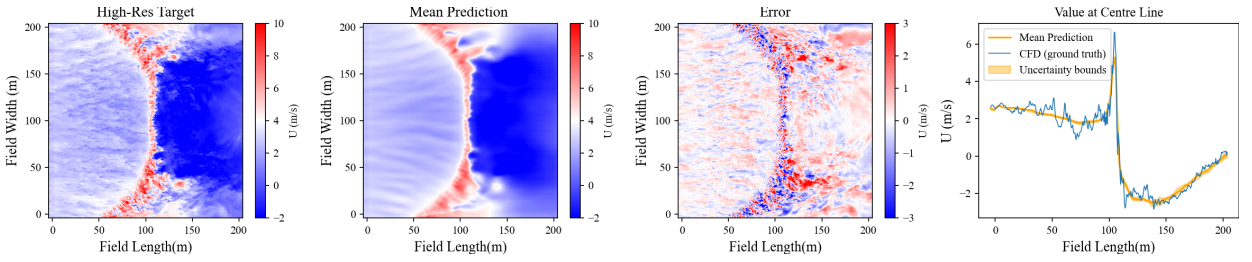

(a) Measurement noise= 0%

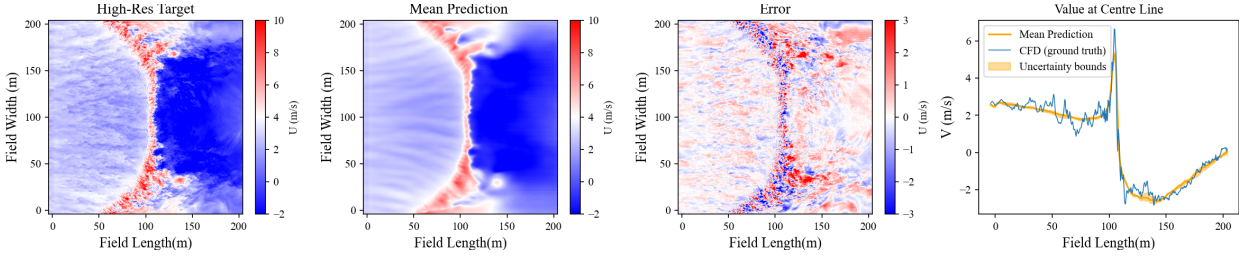

(b) Measurement noise= 10%

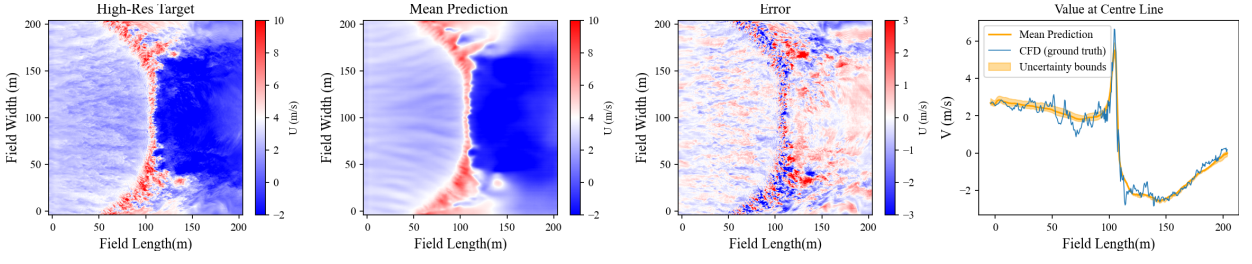

(c) Measurement noise= 30%

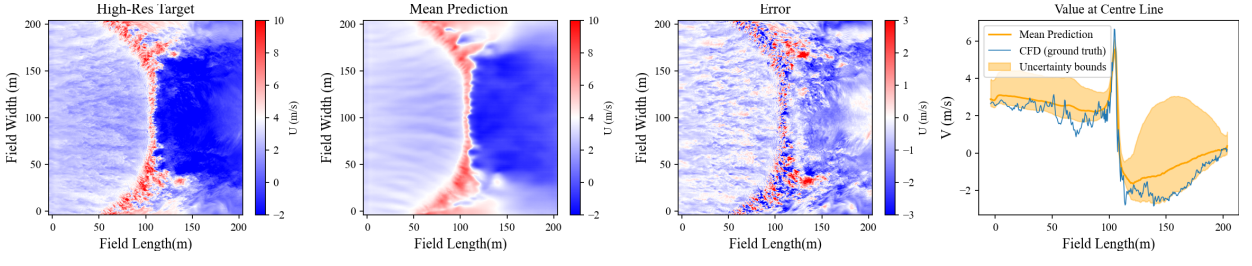

(d) Measurement noise= 50%

Figure 11: Results of the near-surface U-component of wind velocity estimation for case 49(3), $u_{10} = 4$ m/s, $H_g = 0.2$ m and $S = 0\%$, under different measurement noise levels, showing the high-resolution ground truth/target, the model's mean prediction, the reconstruction error, and a comparison of the estimated value along the centerline of the field with the ground truth (CFD)

These drawbacks point to opportunities where further study can improve the system and make it more flexible for use in real-world situations. The proposed technique has the potential to be useful for research projects as well as fire management and suppression tactics with additional development.

6. Conclusions

This study proposes a novel framework based on a combination of real-time UAV-swarm-based measurements of the fire-induced wind field with Deep learning techniques for downscaling wind observations from measurement height to the near-surface level at the desired spatial resolution. A total of 150 three-dimensional simulations of the grassland

fire propagation are performed using the Fire Dynamics Simulator (FDS) software with different wind speeds, terrain slope, and vegetation type and heights to provide a synthetic dataset for training the DL models.

The wind field at two different heights of 40m *AGL* and 2m *AGL* are extracted from the model at different intervals throughout the fire propagation and are used as input and target pairs to train an attention-based residual model. A two-step framework is developed with the overall aim of mapping the sparsely sensed high altitude wind field at 40m *AGL* into the near surface wind field at 2m *AGL* at different stages of the fire propagation.

The trained model is then evaluated against varying swarm sizes, spatial distribution of UAVs, and different ratios of noise in the input values. Results indicate that the proposed framework is capable of providing fast and accurate estimations of the three-dimensional velocity components of the near-surface wind. The trained model achieved the overall MAE and RMSE values of 0.321 m/s and 0.644 m/s, respectively, for $U \in$[-7.42, 31.46], 0.219 and 0.499 for $V \in$[-20.41,19.83]), and 0.147 and 0.430 for $W \in$[-17,32,12.90] which indicates that the errors are not significant compared to the range of the velocities variations. It is also indicated that the model is robust against input noise and shows satisfactory performance against unseen and limited swarm sizes. Considering that the wind measurement using UAVs could include significant levels of noise, the model is then tested against different ratios of input Gaussian noise of up to 50%. The obtained results indicated that even though the output results become so noisy, the model is still capable of estimating the average behaviour of the wind field even against high levels of input noise of up to 30%. This confirms its potential in real-world UAV-based measurement systems, where noisy data is common, and emphasises its capability for generalisation to unseen scenarios.

CRediT authorship contribution statement

Mohammad Tavakol Sadrabadi: Conceptualisation, Methodology, Software, Writing, Investigation, Visualisation. **Mauro Sebastián Innocente:** Conceptualisation, Methodology, Software, Writing, Supervision, Resources, Visualisation.

References

[1] J. T. Abatzoglou, A. P. Williams, Impact of anthropogenic climate change on wildfire across western us forests, Proceedings of the National Academy of Sciences 113 (42) (2016) 11770–11775. doi:doi:10.1073/pnas.1607171113.
URL https://www.pnas.org/doi/abs/10.1073/pnas.1607171113

[2] N. J. Abram, B. J. Henley, A. Sen Gupta, T. J. R. Lippmann, H. Clarke, A. J. Dowdy, J. J. Sharples, R. H. Nolan, T. Zhang, M. J. Wooster, J. B. Wurtzel, K. J. Meissner, A. J. Pitman, A. M. Ukkola, B. P. Murphy, N. J. Tapper, M. M. Boer, Connections of climate change and variability to large and extreme forest fires in southeast australia, Communications Earth and Environment 2 (1) (2021) 8. doi:10.1038/s43247-020-00065-8.
URL https://doi.org/10.1038/s43247-020-00065-8

[3] B. E. Potter, Atmospheric interactions with wildland fire behaviour – i. basic surface interactions, vertical profiles and synoptic structures, International Journal of Wildland Fire 21 (7) (2012) 779–801. doi:https://doi.org/10.1071/WF11128.
URL https://www.publish.csiro.au/paper/WF11128

[4] B. E. Potter, Atmospheric interactions with wildland fire behaviour – 2. plume and vortex dynamics, International Journal of Wildland Fire 21 (7) (2012) 802–817. doi:https://doi.org/10.1071/WF11129.
URL https://www.publish.csiro.au/paper/WF11128

[5] H. T. Gisborne, Measuring forest-fire danger in northern idaho, Report (1928).

[6] N. Liu, J. Lei, W. Gao, H. Chen, X. Xie, Combustion dynamics of large-scale wildfires, Proceedings of the Combustion Institute 38 (1) (2021) 157–198. doi:https://doi.org/10.1016/j.proci.2020.11.006.
URL https://www.sciencedirect.com/science/article/pii/S1540748920307057

[7] J.-L. Dupuy, R. R. Linn, V. Konovalov, F. Pimont, J. A. Vega, E. Jiménez, Exploring three-dimensional coupled fire–atmosphere interactions downwind of wind-driven surface fires and their influence on backfires using the higrad-firetec model, International Journal of Wildland Fire 20 (6) (2011) 734–750. doi:https://doi.org/10.1071/WF10035.
URL https://www.publish.csiro.au/paper/WF10035

[8] J. Zhang, M. Katurji, P. Zawar-Reza, T. Strand, The role of helicity and fire–atmosphere turbulent energy transport in potential wildfire behaviour, International Journal of Wildland Fire 32 (1) (2023) 29–42. doi:https://doi.org/10.1071/WF22101.
URL https://www.publish.csiro.au/paper/WF22101

[9] M. Tavakol Sadrabadi, M. S. Innocente, E. Gkanas, I. Papagiannis, Comparison of the effect of one-way and two-way fire-wind coupling on the modelling of wildland fire propagation dynamics (2022). doi:DOI:10.14195/978-989-26-2298-9_18.

[10] B. J. Stocks, M. E. Alexander, R. A. Lanoville, Overview of the international crown fire modelling experiment (icfme), Canadian Journal of Forest Research 34 (8) (2004) 1543–1547. doi:10.1139/x04-905.
URL https://cdnsciencepub.com/doi/abs/10.1139/x04-905

[11] M. Katurji, B. Noonan, J. Zhang, A. Valencia, B. Schumacher, J. Kerr, T. Strand, G. Pearce, P. Zawar-Reza, Atmospheric turbulent structures and fire sweeps during shrub fires and implications for flaming zone behaviour, International Journal of Wildland Fire 32 (1) (2023) 43–55.

doi:https://doi.org/10.1071/WF22100.
URL https://www.publish.csiro.au/paper/WF22100

[12] A. Desai, S. Goodrick, T. Banerjee, Investigating the turbulent dynamics of small-scale surface fires, Scientific Reports 12 (1) (2022) 10503. doi:10.1038/s41598-022-13226-w.
URL https://doi.org/10.1038/s41598-022-13226-w

[13] J. Innocent, D. Sutherland, N. Khan, K. Moinuddin, Physics-based simulations of grassfire propagation on sloped terrain at field scale: motivations, model reliability, rate of spread and fire intensity, International Journal of Wildland Fire (2023) –doi:https://doi.org/10.1071/WF21124.
URL https://www.publish.csiro.au/paper/WF21124

[14] A. M. G. Lopes, L. M. Ribeiro, D. X. Viegas, J. R. Raposo, Simulation of forest fire spread using a two-way coupling algorithm and its application to a real wildfire, Journal of Wind Engineering and Industrial Aerodynamics 193 (2019) 103967. doi:https://doi.org/10.1016/j.jweia.2019.103967.
URL https://www.sciencedirect.com/science/article/pii/S0167610519305653

[15] M. Vanella, K. McGrattan, R. McDermott, G. Forney, W. Mell, E. Gissi, P. Fiorucci, A multi-fidelity framework for wildland fire behavior simulations over complex terrain, Atmosphere 12 (2) (2021) 273.
URL https://www.mdpi.com/2073-4433/12/2/273

[16] A. Bakhshaii, E. Johnson, A review of a new generation of wildfire–atmosphere modeling, Canadian Journal of Forest Research 49 (6) (2019) 565–574. doi:https://doi.org/10.1139/cjfr-2018-0138.

[17] R. Linn, J. Reisner, J. J. Colman, J. Winterkamp, Studying wildfire behavior using firetec, International Journal of Wildland Fire 11 (4) (2002) 233–246. doi:https://doi.org/10.1071/WF02007.
URL https://www.publish.csiro.au/paper/WF02007

[18] W. E. Mell, M. A. Jenkins, J. S. Gould, P. B. Cheney, A physics-based approach to modelling grassland fires, International Journal of Wildland Fire 16 (2007) 1–22. doi:https://doi.org/10.1071/WF06002.

[19] M. A. Finney, Farsite: Fire area simulator-model development and evaluation (1998). doi:https://doi.org/10.2737/RMRS-RP-4.

[20] P. L. Andrews, Current status and future needs of the behaveplus fire modeling system., International Journal of Wildland Fire. 23 (2014) 21–33. doi:https://doi.org/10.1071/WF12167.

[21] P. Grasso, M. Innocente, A two-dimensional reaction-advection-diffusion model of the spread of fire in wildlands., in: Advances in Forest Fire Research, pp. 334–342. doi:https://doi.org/10.14195/978-989-26-16-506_36.

[22] P. Grasso, M. S. Innocente, Physics-based model of wildfire propagation towards faster-than-real-time simulations, Computers & Mathematics with Applications 80 (5) (2020) 790–808. doi:https://doi.org/10.1016/j.camwa.2020.05.009.
URL https://www.sciencedirect.com/science/article/pii/S0898122120302078

[23] T. Srivas, T. Artés, R. A. de Callafon, I. Altintas, Wildfire spread prediction and assimilation for farsite using ensemble kalman filtering1, Procedia Computer Science 80 (2016) 897–908. doi:https://doi.org/10.1016/j.procs.2016.05.328.
URL https://www.sciencedirect.com/science/article/pii/S187705091630727X

[24] N. S. Wagenbrenner, J. M. Forthofer, B. K. Lamb, K. S. Shannon, B. W. Butler, Downscaling surface wind predictions from numerical weather prediction models in complex terrain with windninja, Atmospheric Chemistry and Physics 16 (8) (2016) 5229–5241, aCP. doi:10.5194/acp-16-5229-2016.
URL https://acp.copernicus.org/articles/16/5229/2016/

[25] K. Höhlein, M. Kern, T. Hewson, R. Westermann, A comparative study of convolutional neural network models for wind field downscaling, Journal of Meteorological Applications 27 (6) (2020) e1961. doi:https://doi.org/10.1002/met.1961.
URL https://rmets.onlinelibrary.wiley.com/doi/abs/10.1002/met.1961

[26] J. M. Forthofer, B. W. Butler, N. S. Wagenbrenner, A comparison of three approaches for simulating fine-scale surface winds in support of wildland fire management. part i. model formulation and comparison against measurements, International Journal of Wildland Fire 23 (7) (2014) 969–981. doi:https://doi.org/10.1071/WF12089.
URL https://www.publish.csiro.au/paper/WF12089

[27] J. M. Forthofer, B. W. Butler, N. S. Wagenbrenner, A comparison of three approaches for simulating fine-scale surface winds in support of wildland fire management. part i.an exploratory study of the effect of simulated winds on fire growth simulations, International Journal of Wildland Fire 23 (7) (2014) 969–981. doi:https://doi.org/10.1071/WF12090.
URL https://www.publish.csiro.au/paper/WF12090

[28] J. Forthofer, K. Shannon, B. Butler, simulating diurnally driven slope winds with windninja, Report (2009).

[29] J. Hilton, N. Garg, Rapid wind–terrain correction for wildfire simulations, International Journal of Wildland Fire 30 (6) (2021) 410–427. doi:https://doi.org/10.1071/WF20062.
URL https://www.publish.csiro.au/paper/WF20062

[30] D. A. Sachindra, F. Huang, A. Barton, B. J. C. Perera, Statistical downscaling of general circulation model outputs to precipitation—part 2: bias-correction and future projections, International Journal of Climatology 34 (11) (2014) 3282–3303. doi:https://doi.org/10.1002/joc.3915.
URL https://rmets.onlinelibrary.wiley.com/doi/abs/10.1002/joc.3915

[31] J. Zhang, X. Zhao, Spatiotemporal wind field prediction based on physics-informed deep learning and lidar measurements, Applied Energy 288 (2021) 116641. doi:https://doi.org/10.1016/j.apenergy.2021.116641.
URL https://www.sciencedirect.com/science/article/pii/S0306261921001732

[32] J. Dujardin, M. Lehning, Wind-topo: Downscaling near-surface wind fields to high-resolution topography in highly complex terrain with deep learning 148 (744) (2022) 1368–1388. doi:https://doi.org/10.1002/qj.4265.
URL https://rmets.onlinelibrary.wiley.com/doi/abs/10.1002/qj.4265

[33] K. Stengel, A. Glaws, D. Hettinger, R. N. King, Adversarial super-resolution of climatological wind and solar data, Proceedings of the National Academy of Sciences 117 (29) (2020) 16805. doi:10.1073/pnas.1918964117.
URL http://www.pnas.org/content/117/29/16805.abstract

[34] J. Cheng, J. Liu, Z. Xu, C. Shen, Q. Kuang, Generating high-resolution climate prediction through generative adversarial network, Procedia Computer Science 174 (2020) 123–127. doi:https://doi.org/10.1016/j.procs.2020.06.067.
URL https://www.sciencedirect.com/science/article/pii/S1877050920315817

[35] K. Fukami, K. Fukagata, K. Taira, Super-resolution analysis via machine learning: a survey for fluid flows, Theoretical and Computational Fluid Dynamics 37 (4) (2023) 421–444. doi:10.1007/s00162-023-00663-0.
URL https://doi.org/10.1007/s00162-023-00663-0

[36] K. Fukami, K. Fukagata, K. Taira, Super-resolution reconstruction of turbulent flows with machine learning, Journal of Fluid Mechanics 870 (2019) 106–120. doi:10.1017/jfm.2019.238.

[37] J. Zhang, J. Liu, Z. Huang, Improved deep learning method for accurate flow field reconstruction from sparse data, Ocean Engineering 280 (2023) 114902. doi:https://doi.org/10.1016/j.oceaneng.2023.114902.
URL https://www.sciencedirect.com/science/article/pii/S0029801823012866

[38] P. Dubois, T. Gomez, L. Planckaert, L. Perret, Machine learning for fluid flow reconstruction from limited measurements, Journal of Computational Physics 448 (2022) 110733. doi:https://doi.org/10.1016/j.jcp.2021.110733.
URL https://www.sciencedirect.com/science/article/pii/S0021999121006288

[39] L. Wang, M. Chen, Z. Luo, B. Zhang, J. Xu, Z. Wang, A. C. Tan, Dynamic wake field reconstruction of wind turbine through physics-informed neural network and sparse lidar data, Energy 291 (2024) 130401. doi:https://doi.org/10.1016/j.energy.2024.130401.
URL https://www.sciencedirect.com/science/article/pii/S0360544224001725

[40] M. Abdar, F. Pourpanah, S. Hussain, D. Rezazadegan, L. Liu, M. Ghavamzadeh, P. Fieguth, X. Cao, A. Khosravi, U. R. Acharya, V. Makarenkov, S. Nahavandi, A review of uncertainty quantification in deep learning: Techniques, applications and challenges, Information Fusion 76 (2021) 243–297. doi:https://doi.org/10.1016/j.inffus.2021.05.008.
URL https://www.sciencedirect.com/science/article/pii/S1566253521001081

[41] A. M. Collins, P. Rivera-Casillas, S. Dutta, O. M. Cecil, A. C. Trautz, M. W. Farthing, Super-resolution and uncertainty estimation from sparse sensors of dynamical physical systems, Frontiers in Water 5 (2023). doi:10.3389/frwa.2023.1137110.
URL https://www.frontiersin.org/journals/water/articles/10.3389/frwa.2023.1137110

[42] Y. Gal, Z. Ghahramani, Dropout as a bayesian approximation: Representing model uncertainty in deep learning (2016). arXiv:1506.02142.
URL https://arxiv.org/abs/1506.02142

[43] M. Teye, H. Azizpour, K. Smith, Bayesian uncertainty estimation for batch normalized deep networks (2018). arXiv:1802.06455.
URL https://arxiv.org/abs/1802.06455

[44] M. S. Innocente, P. Grasso, Self-organising swarms of firefighting drones: Harnessing the power of collective intelligence in decentralised multi-robot systems, Journal of Computational Science 34 (2019) 80–101. doi:https://doi.org/10.1016/j.jocs.2019.04.009.
URL https://www.sciencedirect.com/science/article/pii/S1877750318310238

[45] M. A. Akhloufi, A. Couturier, N. A. Castro, Unmanned aerial vehicles for wildland fires: Sensing, perception, cooperation and assistance, drones 5 (1) (2021) 15. doi:https://doi.org/10.3390/drones5010015.
URL https://www.mdpi.com/2504-446X/5/1/15

[46] W. Thielicke, W. Hübert, U. Müller, M. Eggert, P. Wilhelm, Towards accurate and practical drone-based wind measurements with an ultrasonic anemometer, Atmospheric Measurement Techniques 14 (2) (2021) 1303–1318, aMT. doi:https://doi.org/10.5194/amt-14-1303-2021.
URL https://amt.copernicus.org/articles/14/1303/2021/

[47] N. Vasiljević, M. Harris, A. Tegtmeier Pedersen, G. Rolighed Thorsen, M. Pitter, J. Harris, K. Bajpai, M. Courtney, Wind sensing with drone-mounted wind lidars: proof of concept, Atmospheric Measurement Techniques 13 (2) (2020) 521–536, aMT. doi:https://doi.org/10.5194/amt-13-521-2020.
URL https://amt.copernicus.org/articles/13/521/2020/

[48] K. Sasaki, M. Inoue, T. Shimura, M. Iguchi, In situ, rotor-based drone measurement of wind vector and aerosol concentration in volcanic areas, Atmosphere 12 (3) (2021) 376. doi:https://doi.org/10.3390/atmos12030376.
URL https://www.mdpi.com/2073-4433/12/3/376

[49] T. Wetz, N. Wildmann, F. Beyrich, Distributed wind measurements with multiple quadrotor unmanned aerial vehicles in the atmospheric boundary layer, Atmospheric Measurement Techniques 14 (5) (2021) 3795–3814, aMT. doi:https://doi.org/10.5194/amt-14-3795-2021.
URL https://amt.copernicus.org/articles/14/3795/2021/

[50] S. Prudden, A. Fisher, M. Marino, A. Mohamed, S. Watkins, G. Wild, Measuring wind with small unmanned aircraft systems, Journal of Wind Engineering and Industrial Aerodynamics 176 (2018) 197–210. doi:https://doi.org/10.1016/j.jweia.2018.03.029.
URL https://www.sciencedirect.com/science/article/pii/S016761051730942X

[51] M. Tavakol Sadrabadi, M. S. Innocente, Enhancing wildfire propagation model predictions using aerial swarm-based real-time wind measurements: A conceptual framework, Applied Mathematical Modelling 130 (2024) 615–634. doi:https://doi.org/10.1016/j.apm.2024.03.012.
URL https://www.sciencedirect.com/science/article/pii/S0307904X24001227

[52] G. W. Donnell, J. A. Feight, N. Lannan, J. D. Jacob, Wind characterization using onboard IMU of sUAS, 2018 Atmospheric Flight Mechanics Conference (2018). doi:https://doi.org/10.2514/6.2018-2986.

[53] A. Rautenberg, M. S. Graf, N. Wildmann, A. Platis, J. Bange, Reviewing wind measurement approaches for fixed-wing unmanned aircraft, Atmosphere 9 (11) (2018) 422.

URL https://www.mdpi.com/2073-4433/9/11/422

[54] K. McGrattan, S. Hostikka, J. Floyd, R. McDermott, M. Vanella, E. Mueller, Fire Dynamics Simulator User's Guide, sixth Edition (2023).
URL https://github.com/firemodels/fds/releases/download/FDS-6.8.0/FDS_User_Guide.pdf

[55] N. Cheney, J. Gould, W. Catchpole, The influence of fuel, weather and fire shape variables on fire-spread in grasslands, International Journal of Wildland Fire 3 (1) (1993) 31–44. doi:https://doi.org/10.1071/WF9930031.
URL https://www.publish.csiro.au/paper/WF9930031

[56] C. R. Boardman, M. A. Dietenberger, D. R. Weise, Specific heat capacity of wildland foliar fuels to 434 °c, Fuel 292 (2021) 120396. doi:https://doi.org/10.1016/j.fuel.2021.120396.
URL https://www.sciencedirect.com/science/article/pii/S0016236121002726

[57] A. K. B. Porterie, J. L. Consalvi, J. C. Loraud, Predicting wildland fire behavior and emissions using a fine-scale physical model, Numerical Heat Transfer, Part A: Applications 47 (6) (2005) 571–591. arXiv:https://doi.org/10.1080/10407780590891362, doi:10.1080/10407780590891362.
URL https://doi.org/10.1080/10407780590891362

[58] A. Grishin, Mathematical Modeling of Forest Fires and New Methods of Fighting Them, Publishing House of the Tomsk State University, 1997.
URL https://books.google.co.uk/books?id=JGy-AAAACAAJ

[59] E. Amini, M.-S. Safdari, N. Johnson, D. R. Weise, T. H. Fletcher, Pyrolysis kinetics of wildland vegetation using model-fitting methods, Journal of Analytical and Applied Pyrolysis 157 (2021) 105167. doi:https://doi.org/10.1016/j.jaap.2021.105167.
URL https://www.sciencedirect.com/science/article/pii/S0165237021001534

[60] N. Boonmee, J. Quintiere, Glowing ignition of wood: the onset of surface combustion, Proceedings of the Combustion Institute 30 (2) (2005) 2303–2310. doi:https://doi.org/10.1016/j.proci.2004.07.022.
URL https://www.sciencedirect.com/science/article/pii/S0082078404000268

[61] N. Jarrin, J.-C. Uribe, R. Prosser, D. Laurence, Synthetic inflow boundary conditions for wall bounded flows, Vol. 97 of Notes on Numerical Fluid Mechanics and Multidisciplinary Design, Springer Nature, United States, 2008. doi:10.1007/978-3-540-77815-8_8.

[62] J. Innocent, D. Sutherland, N. Khan, K. Moinuddin, Physics-based simulations of grassfire propagation on sloped terrain at field scale: motivations, model reliability, rate of spread and fire intensity, International Journal of Wildland Fire 32 (2023) 496–512. doi:10.1071/WF21124.

[63] M. Tavakol Sadrabadi, M. S. Innocente, To cut or not to cut: Effect of vegetation height and bulk density on wildfire propagation under varied wind and slope conditions, International Journal of Disaster Risk Reduction 121 (2025) 105372. doi:https://doi.org/10.1016/j.ijdrr.2025.105372.
URL https://www.sciencedirect.com/science/article/pii/S2212420925001967

[64] K. He, X. Zhang, S. Ren, J. Sun, Deep residual learning for image recognition, in: 2016 IEEE Conference on Computer Vision and Pattern Recognition (CVPR), pp. 770–778. doi:10.1109/CVPR.2016.90.

[65] S. Woo, J. Park, J.-Y. Lee, I. S. Kweon, Cbam: Convolutional block attention module, Computer Vision – ECCV 2018, Springer International Publishing, pp. 3–19. doi:10.1007/978-3-030-01234-2_1.

[66] S. Liu, Y. Luo, L. Peng, Y. Jiang, E. Meng, B. Li, Wind pressure field reconstruction based on unbiased conditional kernel density estimation, Journal of Wind Engineering and Industrial Aerodynamics 223 (2022) 104947. doi:https://doi.org/10.1016/j.jweia.2022.104947.
URL https://www.sciencedirect.com/science/article/pii/S0167610522000526

Appendix A. Extra Figures

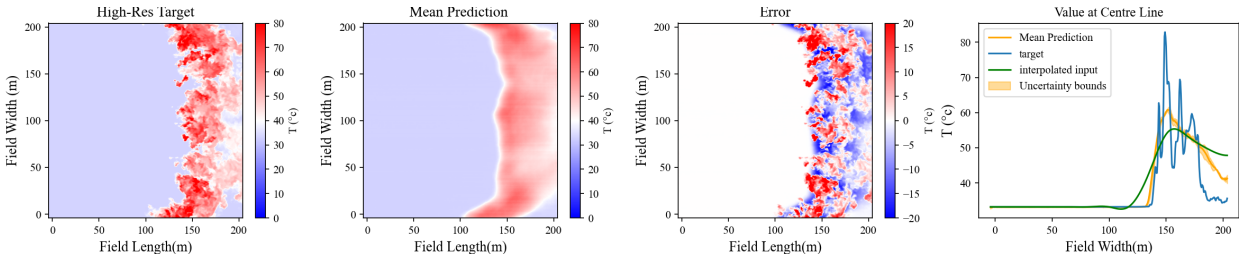

(a) Measurement noise= 0%

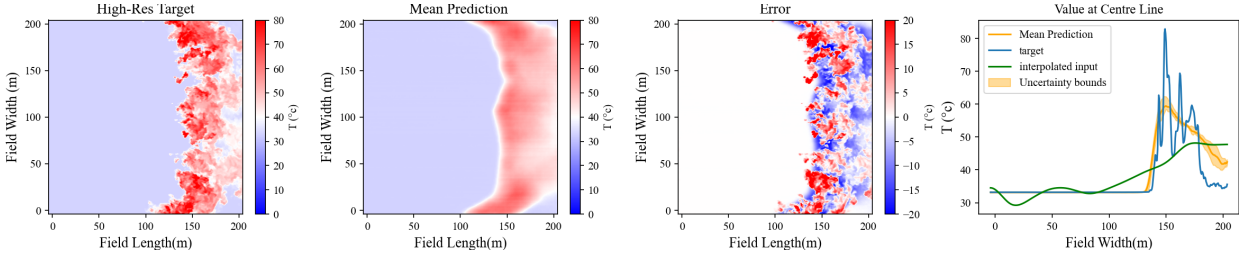

(b) Measurement noise= 10%

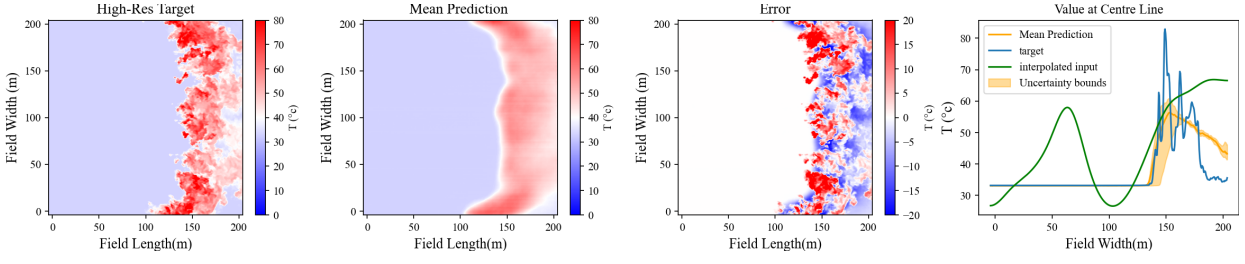

(c) Measurement noise= 30%

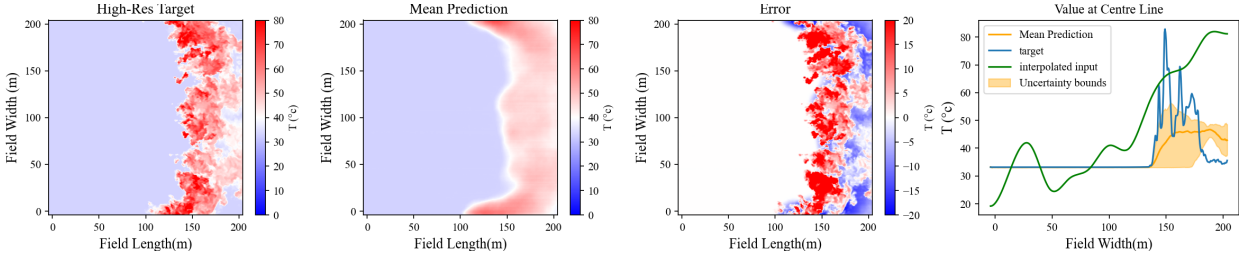

(d) Measurement noise= 50%

Figure 12: 49 (3) -T against different noise levels

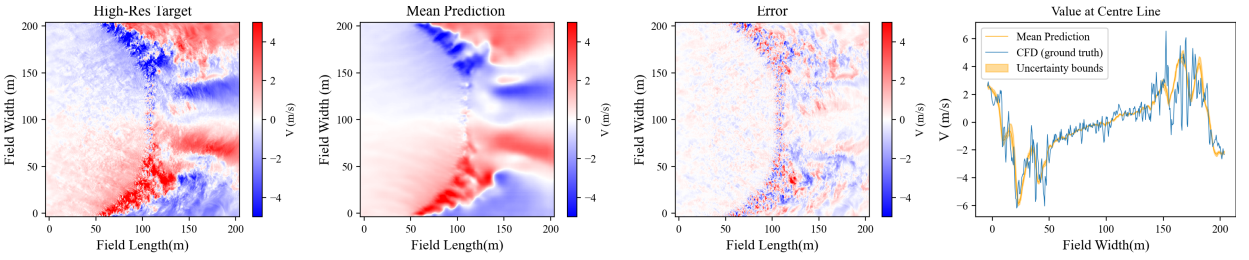

(a) Measurement noise= 0%

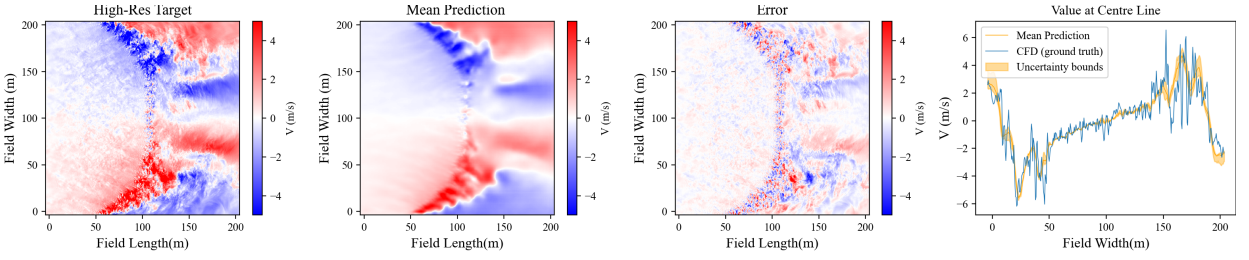

(b) Measurement noise= 50%

Figure 13: Results of the near-surface V-component of wind velocity estimation for case 49(3), $u_{10} = 4$ m/s, $H_g = 0.2$ m and $S = 0\%$, under different measurement noise levels, showing the high-resolution ground truth/target, the model's mean prediction, the reconstruction error, and a comparison of the estimated value along the centerline of the field with the ground truth (CFD)

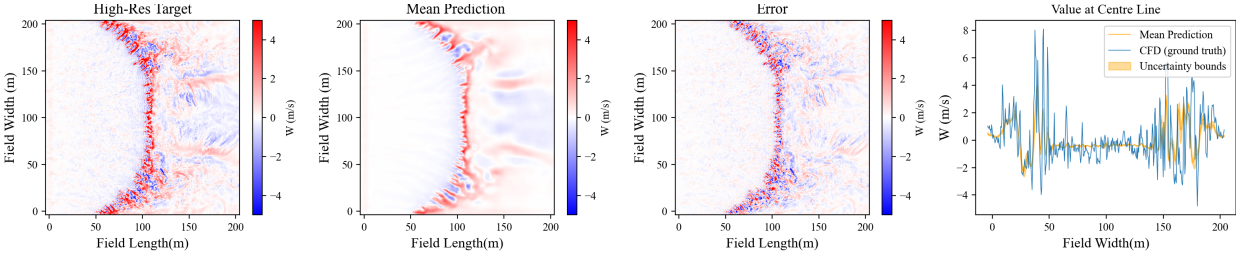

(a) Measurement noise= 0%

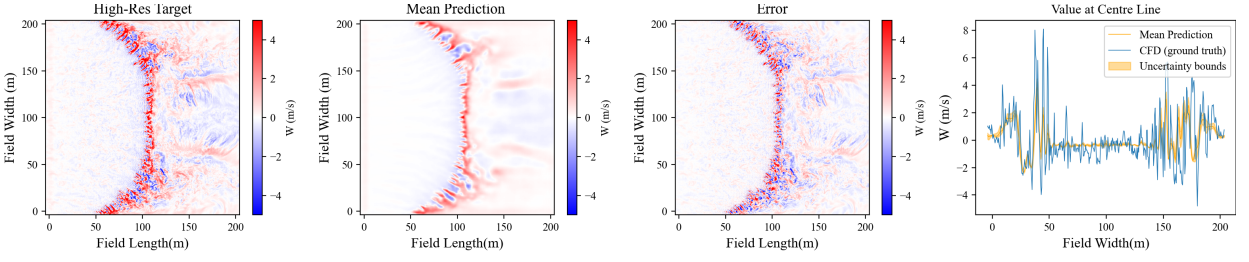

(b) Measurement noise= 50%

Figure 14: Results of the near-surface W-component of wind velocity estimation for case 49(3), $u_{10} = 4$ m/s, $H_g = 0.2$ m and $S = 0\%$, under different measurement noise levels, showing the high-resolution ground truth/target, the model's mean prediction, the reconstruction error, and a comparison of the estimated value along the centerline of the field with the ground truth (CFD)

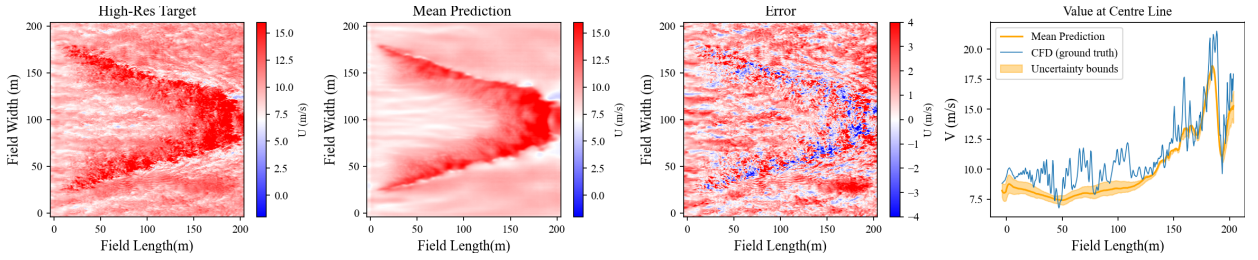

(a) Measurement noise= 0%

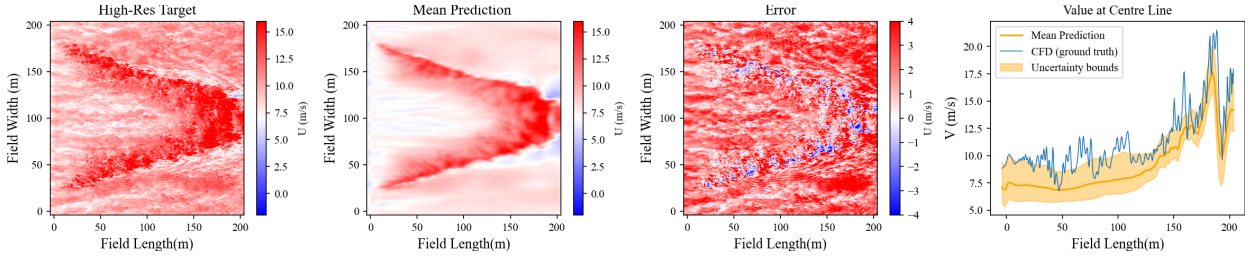

(b) Measurement noise= 50%

Figure 15: Results of the near-surface U-component of wind velocity estimation for case 49(3), $u_{10} = 12$ m/s, $H_g = 0.5$ m and $S = +20\%$, under different measurement noise levels, showing the high-resolution ground truth/target, the model's mean prediction, the reconstruction error, and a comparison of the estimated value along the centerline of the field with the ground truth (CFD)

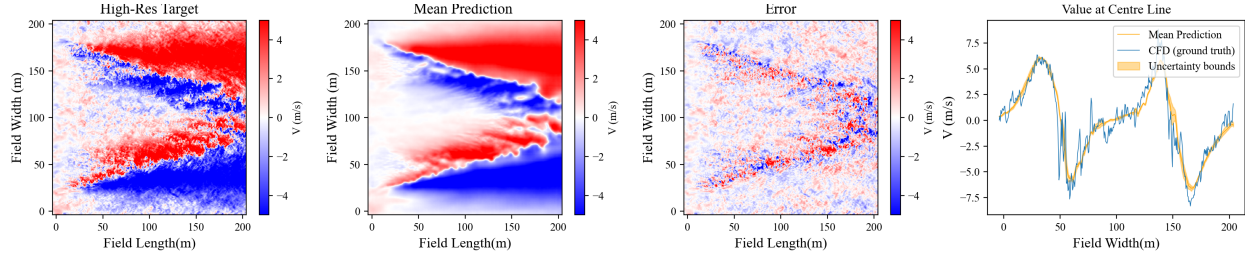

(a) Measurement noise= 0%

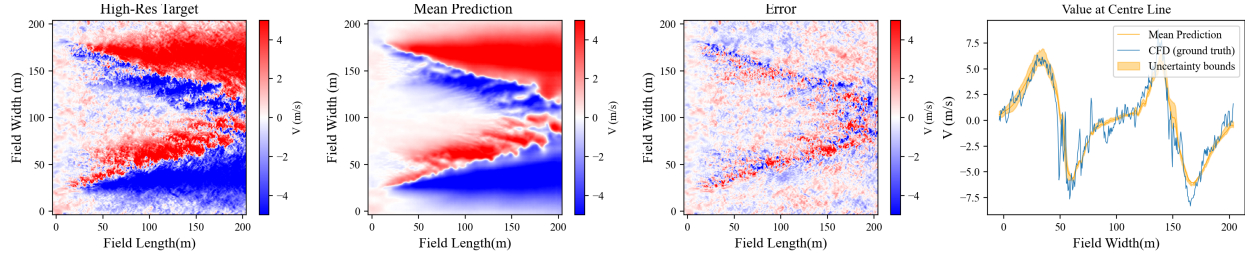

(b) Measurement noise= 50%

Figure 16: Results of the near-surface V-component of wind velocity estimation for case 49(3), $u_{10} = 12$ m/s, $H_g = 0.5$ m and $S = +20\%$, under different measurement noise levels, showing the high-resolution ground truth/target, the model's mean prediction, the reconstruction error, and a comparison of the estimated value along the centerline of the field with the ground truth (CFD)

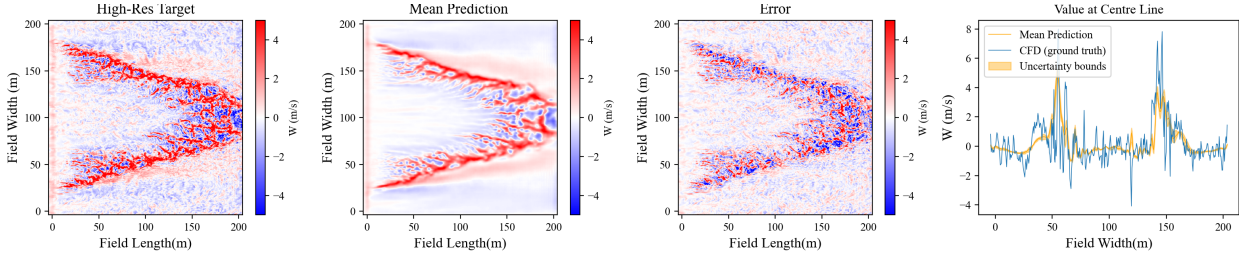

(a) Measurement noise= 0%

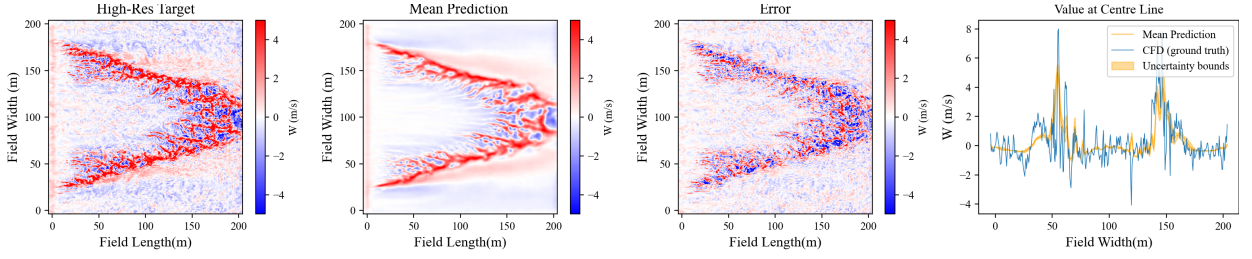

(b) Measurement noise= 50%

Figure 17: Results of the near-surface W-component of wind velocity estimation for case 49(3), $u_{10} = 12$ m/s, $H_g = 0.5$ m and $S = +20\%$, under different measurement noise levels, showing the high-resolution ground truth/target, the model's mean prediction, the reconstruction error, and a comparison of the estimated value along the centerline of the field with the ground truth (CFD)

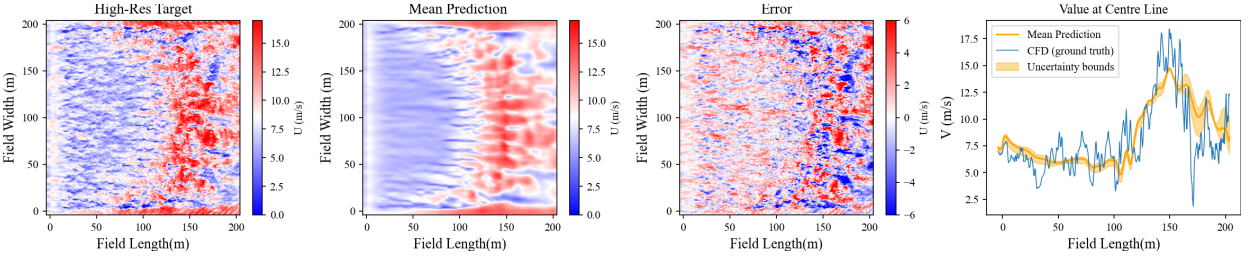

(a) Measurement noise= 0%

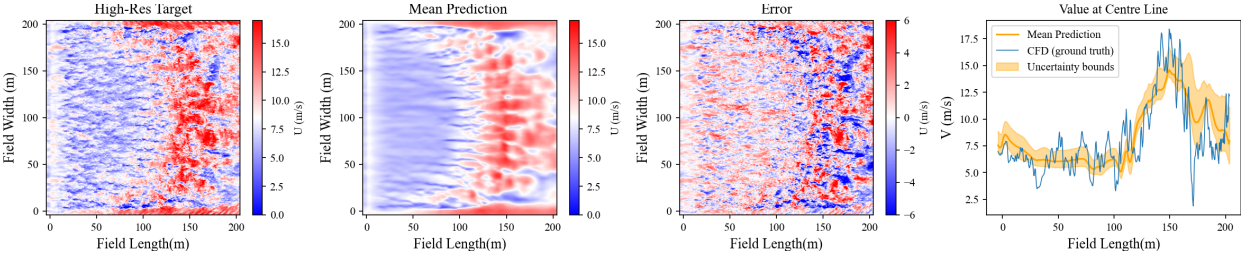

(b) Measurement noise= 50%

Figure 18: Results of the near-surface U-component of wind velocity estimation for case 49(3), $u_{10} = 12$ m/s, $H_g = 1$ m and $S = -20\%$, under different measurement noise levels, showing the high-resolution ground truth/target, the model's mean prediction, the reconstruction error, and a comparison of the estimated value along the centerline of the field with the ground truth (CFD)

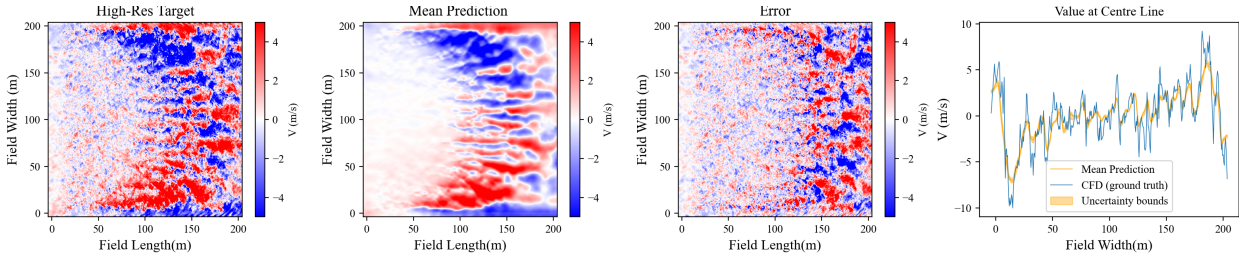

(a) Measurement noise= 0%

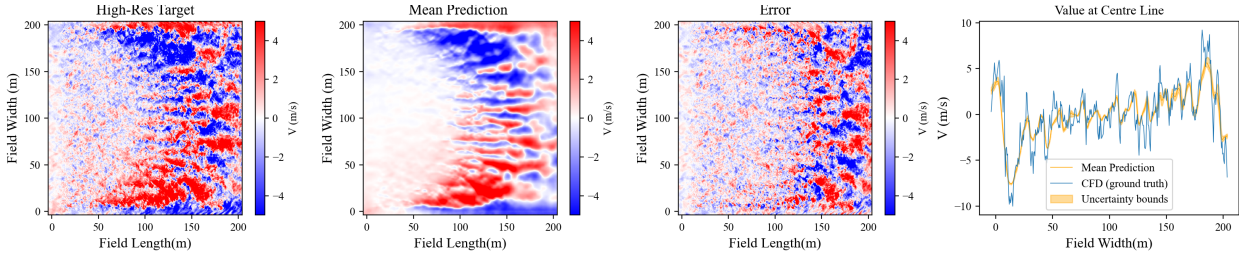

(b) Measurement noise= 50%

Figure 19: Results of the near-surface V-component of wind velocity estimation for case 49(3), $u_{10} = 12$ m/s, $H_g = 1$ m and $S = -20\%$, under different measurement noise levels, showing the high-resolution ground truth/target, the model's mean prediction, the reconstruction error, and a comparison of the estimated value along the centerline of the field with the ground truth (CFD)

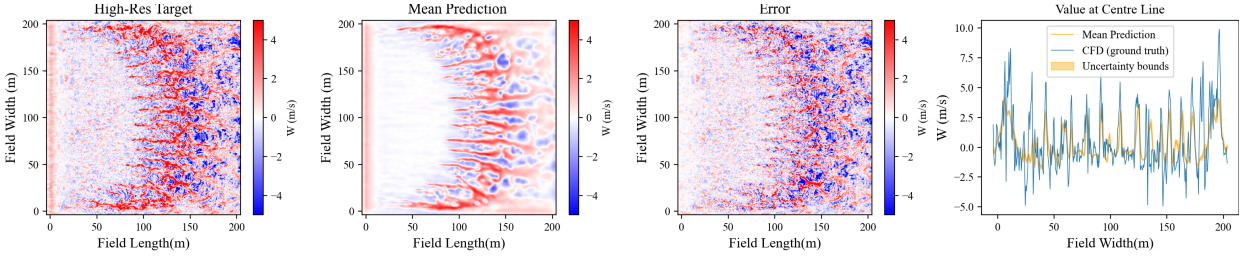

(a) Measurement noise= 0%

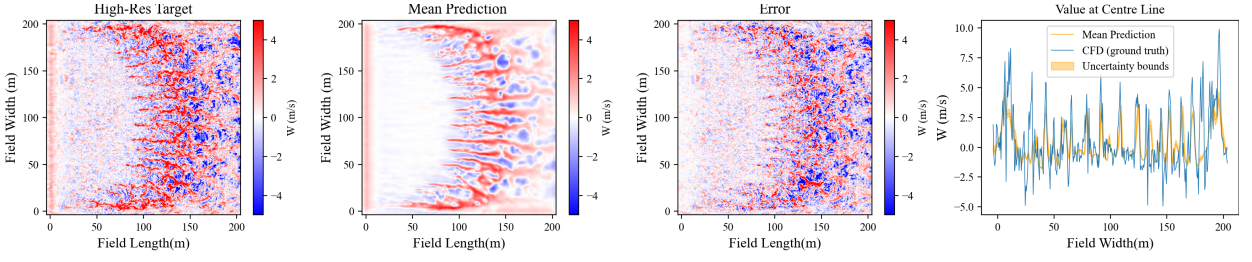

(b) Measurement noise= 50%

Figure 20: Results of the near-surface W-component of wind velocity estimation for case 49(3), $u_{10} = 12$ m/s, $H_g = 1$ m and $S = -20\%$, under different measurement noise levels, showing the high-resolution ground truth/target, the model's mean prediction, the reconstruction error, and a comparison of the estimated value along the centerline of the field with the ground truth (CFD)